Monitoring of the ride-through ability of a 2MW Wind turbine in Tvååker, Halland

Elforsk rapport 09:26

Torbjörn Thiringer, Julia Paixao, Massimo Bongiorno February 2009

Monitoring of ride-through ability of a 2MW Wind turbine in Tvååker, Halland

Elforsk rapport 09:26

Torbjörn Thiringer, Julia Paixao, Massimo Bongiorno February 2009

Förord

The purpose of this project is to verify that a 2 MW DIFG wind turbine manages to ride through severe voltage dips. In addition a goal is derive and present a model of the DFIG turbine equipped with an undervoltage ride-through ability.

The work was carried out by Torbjörn Thiringer, Julia Paixao and Massimo Bongiorno at Chalmers as a project within the Swedish wind energy research programme "Vindforsk – II".

The report is the final report for project V 144.

Vindforsk – II is funded by ABB, the Norwegian based EBL-Kompetense, E.ON Sverige AB, Falkenberg Energi AB, Göteborg Energi, Jämtkraft AB, Karlstad Energi AB, Luleå Energi AB, Lunds Energi AB, Skellefteå Kraft AB, Svenska Kraftnät, Swedish Energy Agency, Tekniska Verken i Linköping AB, Umeå Energi AB, Varberg Energi, Vattenfall AB and Öresundskraft AB.

Comments on the work and the final report have been given by the following persons: Elisabet Norgren, SvK and Philip Kjaer, Vestas.

Sammanfattning

En 2MW Vestas DFIG-vindturbin (ett vindkraftverk utrustad med ett generatorsystem som har en släpringad asynkronmaskin där rotorkretsen är kopplad till en omriktare som är ansluten till elnätet) utrustad med ett system för att hantera svåra nätstörningar har undersökts. Vindkraftverket är utrustad med en s.k. AGO2 (Advanced Grid Option 2)-option som ger denna underspänningsimmunitetsfunktion. En teoretisk modell har byggs och den resulterande funktionaliteten har testats med gott resultat. Endast ett par mindre bromsresistorer med tillhörande kraftelektronik erfordras, ca 10 kg totalt för ett 2MW's verk.

Ett högpresterande mätsystem har installerats och de matande spänningarna såväl som interna spänningar och strömmar samt vidare de till elnätet utgående strömmarna har registrerats kontinuerligt. Under mätperioden som varade från maj 2008 till december 2008 förekom 3 större nätstörningar. Den största innebar att den kvarvarande spänningen sjönk ner till nästan 0 %. Vindkraftverket klarade denna samt samtliga övriga spänningsstörningar som förekom under mätperioden.

Summary

The ride-through functionality of a 2MW DFIG wind turbine equipped with an undervoltage ride-through functionality has been verified directly by measurement. A comparison has been made with simulations generated by theoretical models.

During 7 months of monitoring, several voltage dips occurred, including one severe dip down to almost 0 %. The wind turbine rode through all occurring dips, remaining connected to the system.

A generic model of the DFIG system consisting of publicly available algorithms was formed and implemented into the simulation program PSCAD/EMTDC. Several simulations were performed to illustrate how this model compares with the response of the 2MW wind turbine to voltage dips. A fairly good agreement was observed.

Preface

The authors would like to thank Varberg Energi for allowing Chalmers to utilize their turbine, and Vestas for helping with the installation of measurement modules and assisting with information about the turbine. In particular, Håkan Svensson, Bengt Olofsson, and Carl-Henrik Olsson at Varberg Energi and Pär Larsson at Vestas are gratefully acknowledged for their positive attitude and helpfulness. The authors would also like to thank Anders Andersson, Styr och Mätteknik Sverige AB, for assistance in obtaining additional data from the wind turbine. Last but not least, the authors would like to express their thanks to Magnus Ellsén, Chalmers for his skillful assistance in setting up the measurement system.

Innehåll

Chapter 1

List of Symbols

P_{tot}	total active power out of the turbine
P_s	stator active power
P_r	rotor active power
s	slip
n_r	rotor mechanical speed
n_s	synchronous speed
P_{st}	short-term flicker severity index
P_{lt}	long-term flicker severity index
c_f	flicker coefficient
P_{wt}	rated power of the turbine
N	number of turbines
THD	total harmonic distortion
θ	transformation angle
$\hat{\theta}$	estimation of the transformation angle
$\hat{\omega}_g$	estimation of the grid frequency
k_i	PLL integral gain
k_p	PLL proportional gain
$\mathbf{v_s}$	stator voltage space vector
$\mathbf{v_r}$	rotor voltage space vector
$\mathbf{i_s}$	stator current space vector
$\mathbf{i_r}$	rotor current space vector
$\mathbf{\Psi_s}$	stator flux-linkage space vector
$\mathbf{\Psi_r}$	rotor flux-linkage space vector
R_s	resistance of the stator winding
R_r	resistance of the rotor winding
θ_r	rotor position
ω_r	rotor angular electrical speed
ω_s	stator frequency

ω_2	slip frequency
ω_k	reference coordinate system angular speed
$\mathbf{\Psi_a}$	air-gap flux-linkage space vector
L_m	mutual inductance between the stator and the rotor
$\mathbf{i_m}$	magnetizing current space vector
L_{sl}	stator leakage inductance
L_{rl}	rotor leakage inductance
L_s	stator inductance
L_r	rotor inductance
J	inertia of the machine
ω_{mech}	rotor angular mechanical speed
T_e	electrodynamical torque
T_l	load torque
L_M	Γ-model magnetizing inductance
L_σ	Γ-model rotor inductance
R_R	Γ-model rotor resistance
b	Γ-model coefficent
$\mathbf{v_R}$	Γ-model rotor voltage space vector
$\mathbf{i_R}$	Γ-model rotor current space vector
$\mathbf{\Psi_R}$	Γ-model rotor flux-linkage space vector
v_{dc}	DC-link voltage
R	DC-link crowbar resistor
$i_{crowbar}$	DC-link crowbar current
C	DC-link capacitor
$\mathbf{i_g}$	grid current space vector
$\mathbf{v_g}$	grid voltage space vector
L_f	grid filter inductance
R_f	grid filter resistance
$k_{p_{rcc}}$	rotor current controller proportional gain
α_{rcc}	rotor current controller bandwidth
α_{ac}	stator voltage low-pass filter bandwidth
α_{aco}	stator flux low-pass filter bandwidth
α_{co}	stator flux low-pass filter bandwidth
$k_{p_{gcc}}$	grid current controller proportional gain
α_{gcc}	grid current controller bandwidth
n_{ratio}	grid-side converter transformer ratio
Q_s	stator's reactive power
k_{i_Q}	stator's reactive power controller integral gain
α_{rpc}	reactive power controller bandwidth
v_{dc0}	DC-link voltage initial condition
$k_{p_{dc}}$	DC-link controller proportional gain

α_{dc} DC-link controller bandwidth

Chapter 2

Introduction

Wind turbines are an increasingly common component in power systems today. As a result, wind turbines can not be allowed to disconnect themselves too easily from the electric network. Otherwise, a substantial amount of energy production could be lost, endangering the stability of the power system.

In order to prevent such a situation from occurring, transmission system operators (TSOs) in various countries have set up typical undervoltage waveforms which wind turbines must be able to ride through without disconnecting themselves.

A very successful wind turbine system is the doubly-fed induction generator (DFIG) system. Only a small converter is used in the rotor circuit, and this decreases investment cost as well as losses. So far, a drawback of this system has been that it is very sensitive to grid disturbances because of its small converter, and could only ride through small voltage dips. Recently, an option has been added to this type of turbine that gives it the functionality to also ride through substantial voltage dips. The first such turbines (Vestas 2 MW turbines with AGO2, Advanced Grid Option 2) in Sweden were installed in Tvååker, Halland. These turbines provided a natural opportunity to verify the ride-through functionality.

Accordingly, the purpose of this work has been to verify that a newly installed DFIG wind turbine will manage to ride through serious voltage dips (a temporary voltage reduction). The way to perform such a verification is to monitor the operation of the turbine during a time period of at least six months. An additional goal of this work was to compare the turbine behavior with simulation models based on publicly available algorithms. Finally an objective was to verify that the derived model could handle the "limit dips" set up by the Swedish TSO SvK.

Chapter 3

Presentation of the investigated turbine

The investigated wind turbine is one out of a group of three Vestas 2 MW wind turbines, equipped with the under voltage ride through feature AGO 2.

3.1 Turbine location

The turbines are connected to a 10 kV cable grid which starts at the 130/10 kV transformer station XT151, about 80 km south of Göteborg, close to the community of Tvååker. The area where the turbines are located is called Munkagård and the investigated turbine has the reference Munkagård 3.

In Fig. 3.1 the location of the transformer station, the cable and the three turbines can be observed.

The short-circuit capacity of the transformer station is 268 MVA on the low-voltage side. The cable is an AXCEL240 cable. The distance to the first turbine, Munkagård 3 is approximately 700 meters. This gives a very strong grid connection point of 200 MVA for the Munkagård 3 turbine with a short-circuit impedance angle of 70 degrees.

3.2 General overview of the DFIG system

In Fig. 3.2 the single-line diagram of the investigated DFIG turbine is presented.

The converter located between the rotor circuit of the generator and the electric grid is a key component of the DFIG system. It provides the tur-

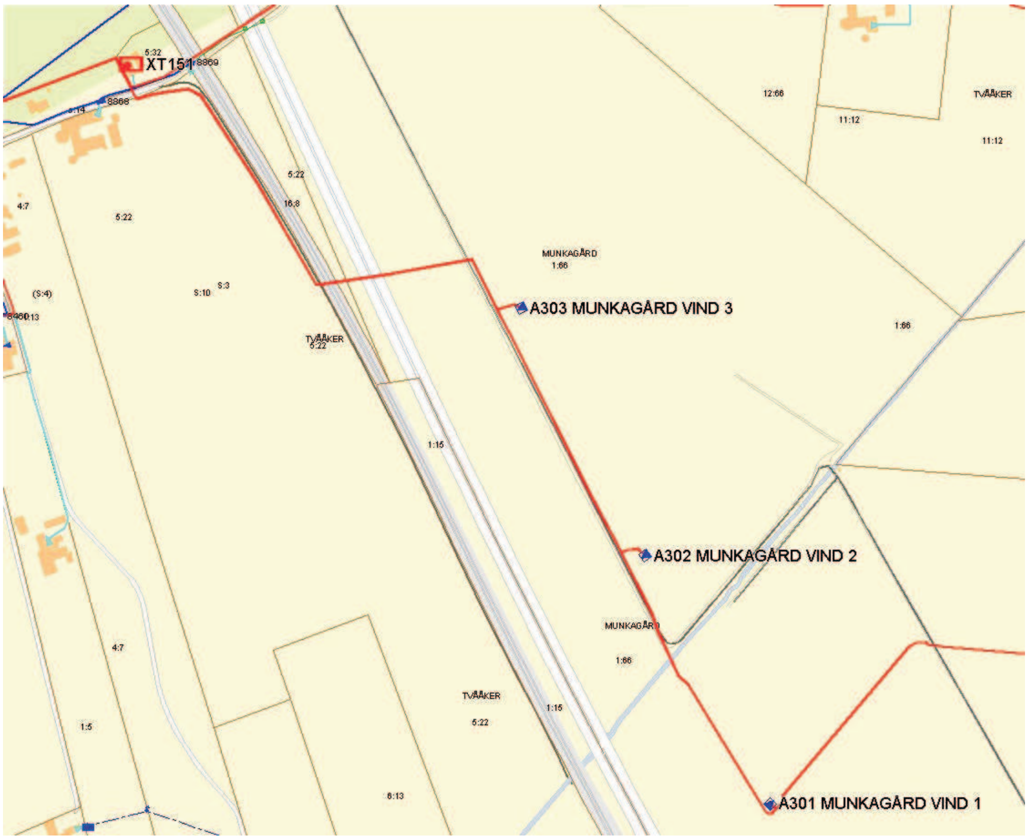

Figure 3.1: The transformer station X151 Tvååker, the cable and the three turbines.

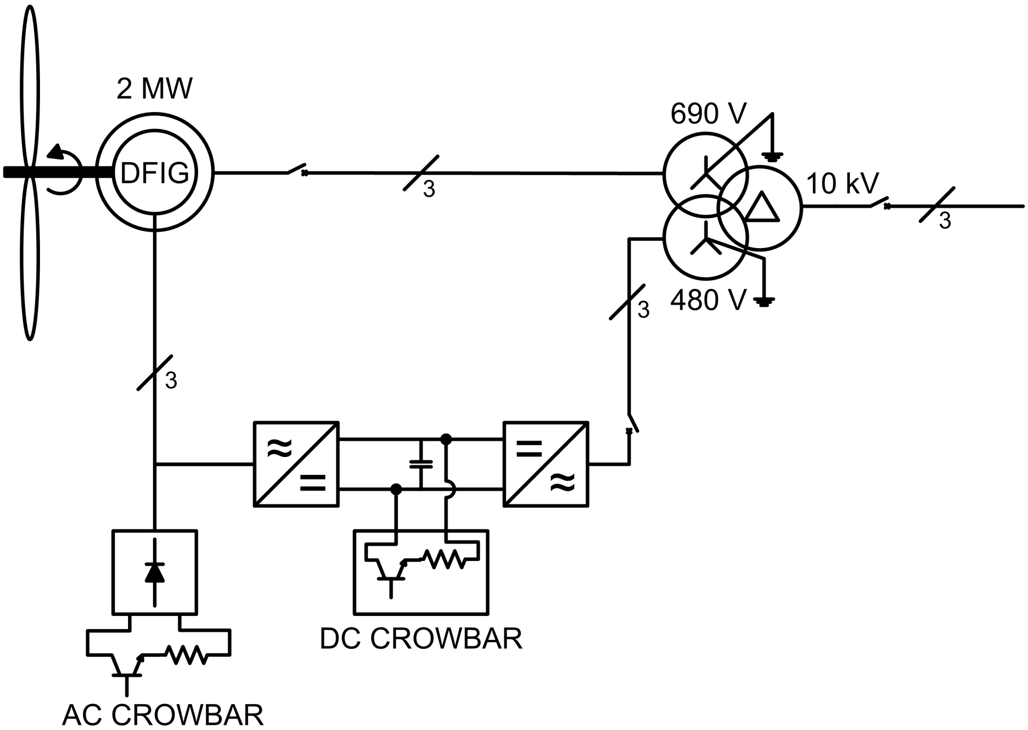

Figure 3.2: Overview of the DFIG system equipped with the ride-through functionality

bine with ”variable-speed advantages” such as a smooth shaft torque and an adjustable reactive power exchange with the grid.

The reason for the great success of the DFIG concept is that in this arrangement, the converter required becomes much smaller as compared to a ”normal” placement, i.e between the generator stator and the grid. Not only does this placement of the converter give the possibility to reduce the cost, it also reduces the power electronic losses. It should be mentioned that the induction generator used in this system will be slightly more expensive compared to a standard induction generator, since it is equipped with a wound rotor and slip rings in the rotor. A standard induction machine has a simpler rotor with casted aluminum bars as windings. Such a standard type of the induction machine is called a cage-bar induction machine.

The drawback of the DFIG system from the power system stability point of view has so far been its inability to ride through severe voltage dips. In order to overcome this drawback, a ride-through ability can be added to this type of turbine, as presented in the next section. Another slight drawback is that, due to the limited converter size, the turbine will get a limited speed range. However, as will be presented in the following chapter, the speed range is quite sufficient.

In order to reduce the magnetizing losses at low wind speed, the turbine operate Y-connected at low wind speeds, and at around 500 kW it switches over to Δ-connection. In principle it means that a smaller generator is used for low wind speeds and a larger for higher wind speed, which saves energy at low wind speeds.

3.3 Ride-through functionality description

There are different variants of ride-through systems for a DFIG wind turbine system. Many use so-called crowbars, i.e low-ohmic resistors (or even no resistors) that can be connected to the circuit using power electronic components in order to drain the system of energy when necessary.

In the investigated system, this is primarily the task of the dc-crowbar presented in Fig. 3.2. Voltage dips coming from disturbances in the power system will unavoidably propagate to the grid side converter and the stator circuit of the DFIG system. For the grid side converter this is no problem, but for the generator, a voltage dip will lead to a demagnetization of the generator, causing large currents and powers to flow in the stator and rotor circuits.

Since the converter was designed to handle only a part of the total power, the ac and dc crowbar are placed in the system to drain the system of excess energy during disturbances. In the turbine studied, this is achieved mainly by using the DC-link crowbar. The rotor side converter diodes have the ability to conduct a large amount of current, but the grid side converter must instead mainly use its transistors to feed the power out to the grid. This means that the grid side converter has a limited apparent power capability of ca 600 kVA, which is not sufficient during heavy power system disturbances. In addition to the limited capability of the converter there is an additional problem, the inflow of energy towards the dc-link happens so quickly that the current controller of the grid side converter has no time to react. As a consequence, the voltage on the DC-link will rise quickly. In this event, the DC-link crowbar activates to drain the DC-link of energy in order to protect the DC-link capacitor as well as the transistors in the converters from overvoltage.

Chapter 4

Steady-state operation characteristics

In parallel to the measurement system set up by Chalmers, Anders Andersson, Styr och Mätteknik Sverige AB, was also operating a measurement system that made measurements of the power, voltage, rotor speed and wind speed on a one second basis. Using this other system, electrical quantities as voltages, currents and powers determined with the Chalmers system could be verified. An additional advantage was that it became possible to obtain values of the wind speed and generator speed that could be used to find the specific operating-points of the turbine.

4.1 General operating characteristics

In Fig. 4.1 the wind speed-electric power characteristic of the turbine is presented.

The results shown have not been completely "cleaned up"; they also show conditions that should have been excluded. It can, however, be inferred that the turbine works well. This is confirmed by the binned and averaged results presented in Fig. 4.2.

The rotor speed versus wind speed is presented in Fig. 4.3. It can be seen that at the lowest power level, the turbine limits rotor speed to a minimum value. This means that it is no longer operating at the optimal efficiency at the very lowest wind speeds. However, the limitation occurs over a small range and for low wind speeds, and results in only a negligible loss in the converted wind energy. The binned and averaged results are presented in Fig. 4.4

The electric power as a function of rotor speed is presented in Fig. 4.5.

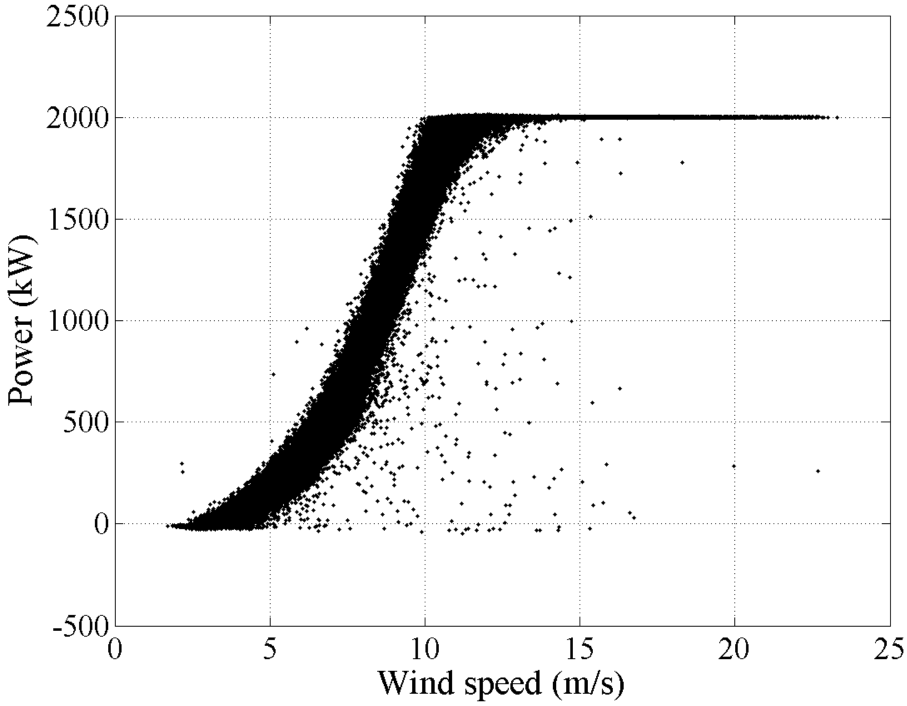

Figure 4.1: Electric power as a function of wind speed, raw measurements, one-minute average values.

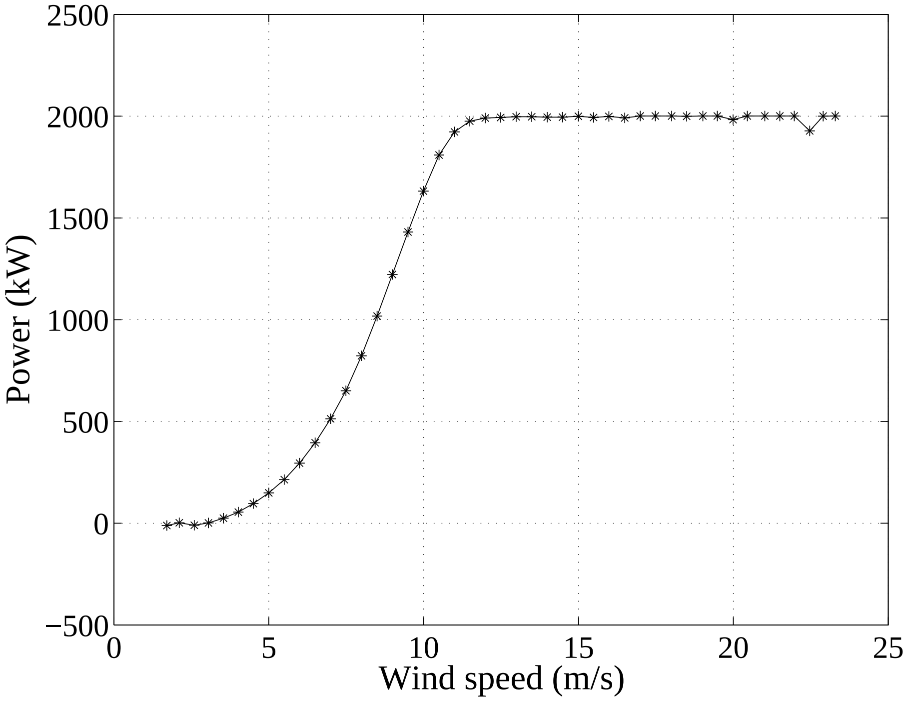

Figure 4.2: Electric power as a function of wind speed, binned and averaged results

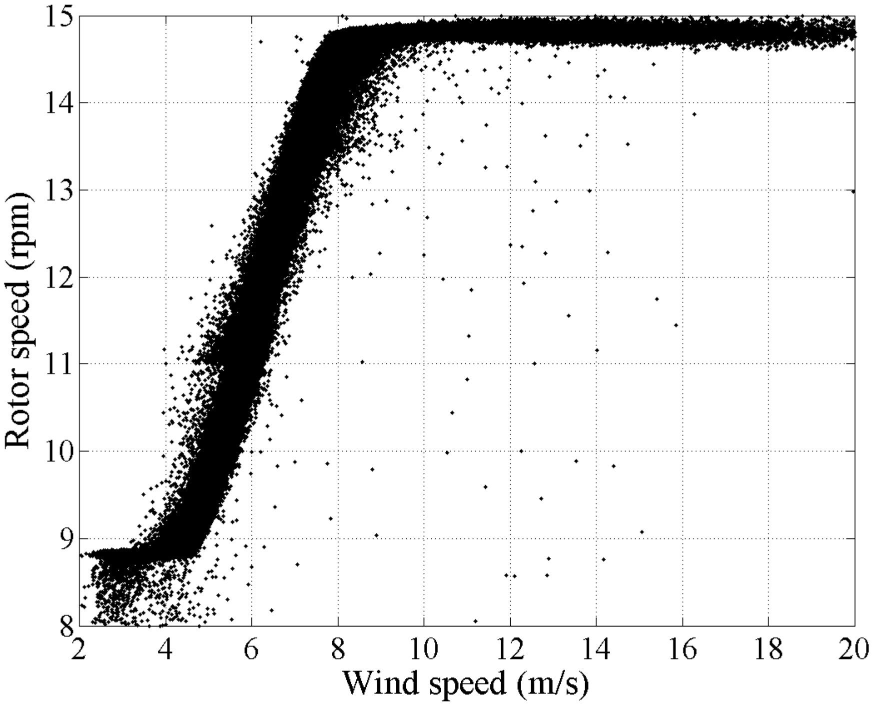

Figure 4.3: Rotor speed as a function of wind speed, raw measurements, one-minute average values.

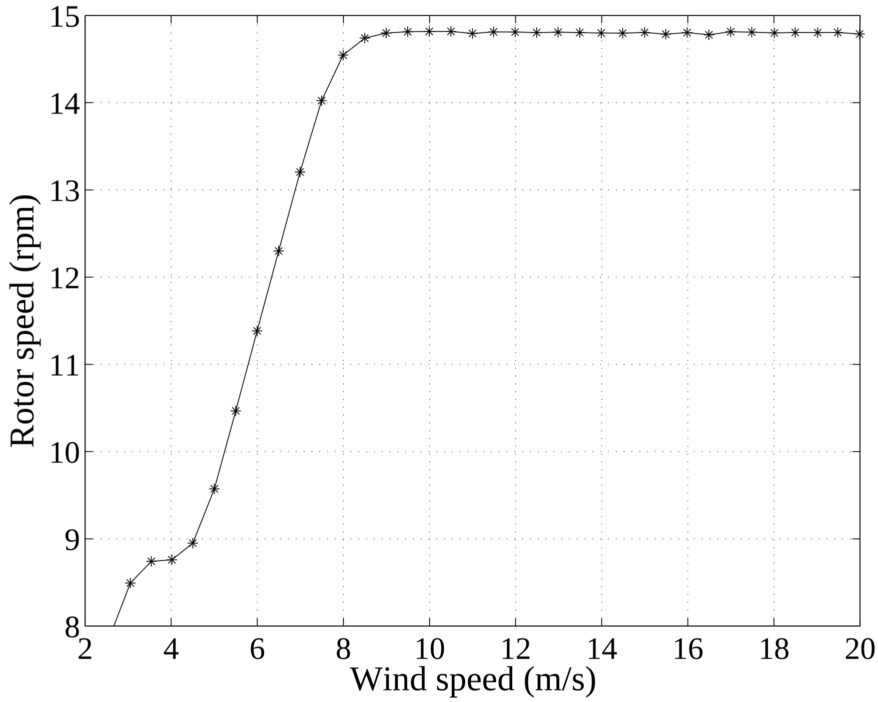

Figure 4.4: Rotor speed as a function of wind speed, binned and averaged results.

Here, the corresponding synchronous speed of the generator (after accounting for the gear-box) has also been drawn. The synchronous speed is the speed with which the generator would rotate if it is connected to the grid and the rotor voltage is held to zero by short-circuiting the rotor slip rings. For this turbine, the synchronous speed is 13.2 rpm. In the DFIG system, the total power out of the turbine is composed of two components,

$$P_{tot} = P_s + P_r \tag{4.1}$$

where P_{tot}, P_s and P_r are the total, stator and rotor powers respectively. When the rotor speed is below the synchronous speed, the rotor power is negative, i.e. power flows in to the rotor. The opposite is true when the rotor speed is above the synchronous speed, which occurs during high wind speeds. The power flowing in the rotor can expressed as a function of the total power and the slip s,

$$P_r = \frac{s}{1-s} P_{tot} \tag{4.2}$$

where s is determined as

$$s = \frac{n_r - n_s}{n_s} \tag{4.3}$$

and n_r and n_s are rotor speed and synchronous speed respectively. The binned and average result is displayed in Fig. 4.6

From Figs. 4.5 and 4.6 it can be observed that at the highest power levels, the speed difference between the generator speed and synchronous speed is rather small, so that only about 15 % of the power flows through the converter. When the wind speed is at its lowest, a fairly large ratio of the total power flows in through the rotor. However, this total power is low and the fraction flowing from the rotor is not enough to thermally overheat the converter. Accordingly, a smaller converter (about 25 % of the rating of the system) can be used.

In order to find the corresponding torque and rotor speed for a given operating point when the disturbances occurred, the relation presented in Fig. 4.7 was used.

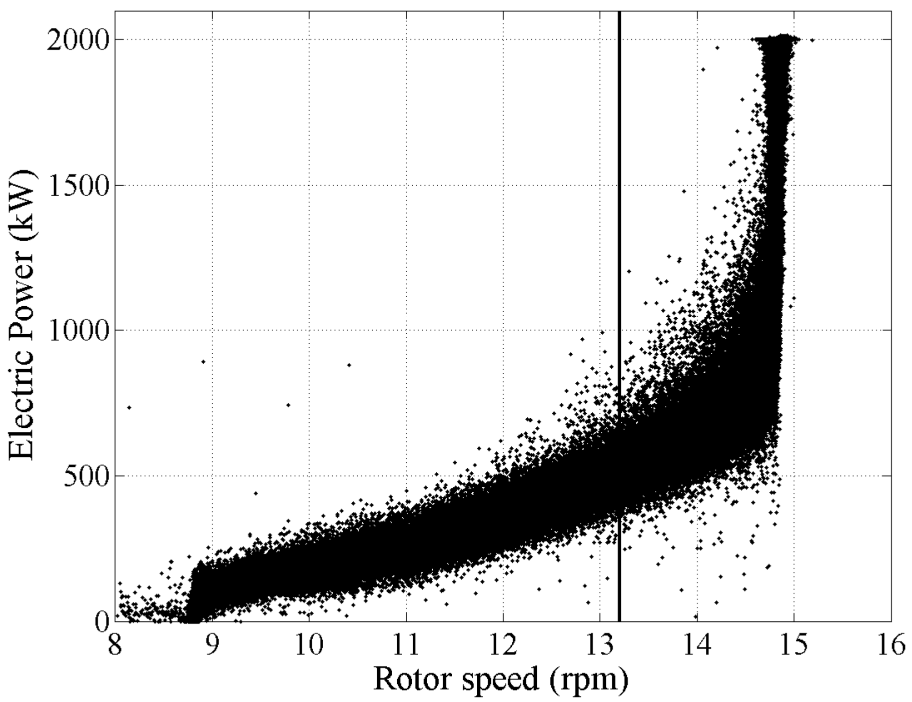

Figure 4.5: Electric power as a function of rotor speed, raw measurements, one-minute average values.

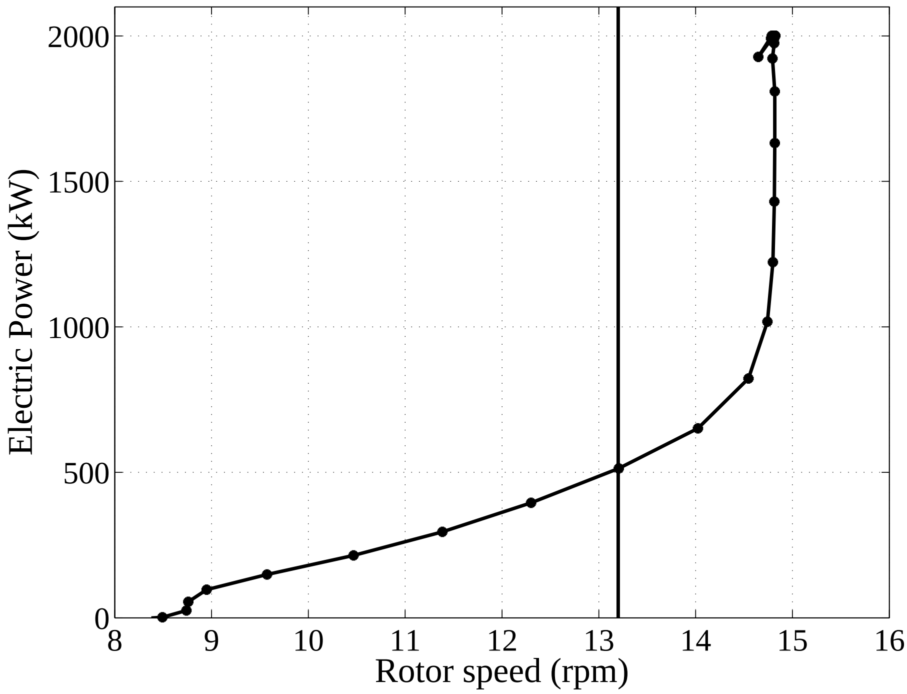

Figure 4.6: Electric power as a function of rotor speed, binned and averaged results.

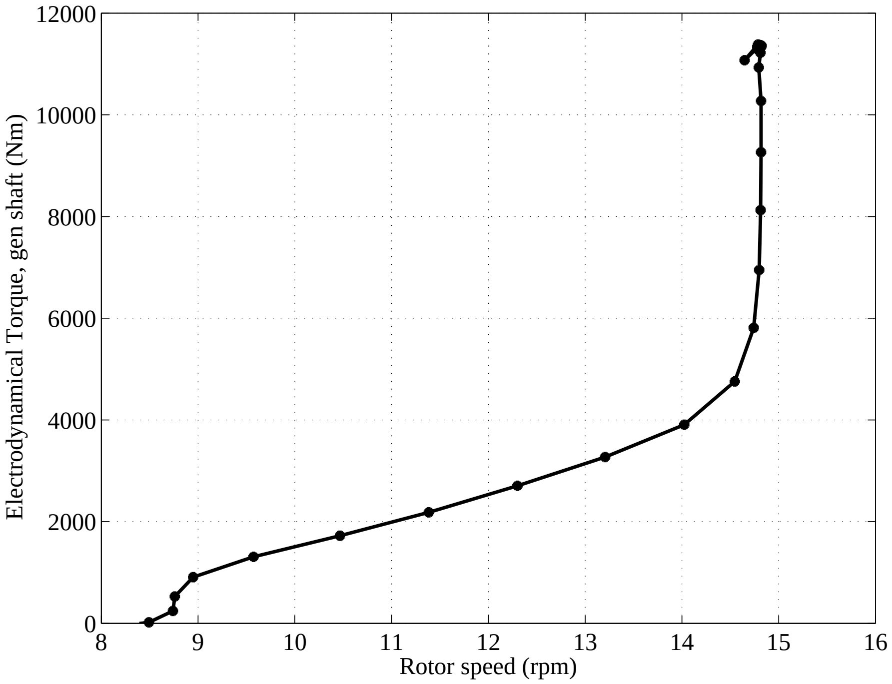

Figure 4.7: Torque as a function of rotor speed.

4.2 Flicker contribution

If the voltage level varies quickly (in the frequency range of 0.1 to 10 Hz) there is a risk that this will cause an annoying "flickering" of an incandescent light. The quantity to characterize this disturbance level is called flicker severity index, P_{st}/P_{lt} (short-term and long-term). If the P_{st}/P_{lt}-value exceeds 1.0, people can be annoyed by the flickering lamps. Accordingly, there is a certain amount of "flicker emission" that objects are allowed to feed into the electric network.

IEC 61400-21 [1] prescribes that the flicker emission from a wind turbine should be determined for a fictitious grid having grid impedance angles of 30, 50, 70 and 85 degrees. The voltage variation that the turbine creates on the fictitius grid can be determined according to

$$\Delta U \approx \frac{P}{U}R_{sc} + \frac{Q}{U}X_{sc} \tag{4.4}$$

where the active and reactive powers from the wind turbine are determined to (7.1) and (7.2). U represents the line to line voltage. The shortcircuit resistance and reactance of the grid, R_{sc} and X_{sc}, are found from the grid strength and grid impedance angle. Using this voltage the procedure stated in [2] can be used.

A flicker coefficient,c_f, that is independent of the selected grid strength, shall be determined. From this coefficient it is possible to determine the flicker impact of a wind installation in advance. Or, in another way, determine what grid strength that is needed to connect a wind installation to the grid. The relation between the flicker coefficient ant the flicker severity index is

$$P_{st} = c_f \frac{P_{wt}}{S_{sc}} \tag{4.5}$$

where S_{sc} is the short-circuit capacity of the grid and P_{wt} is the rating of the turbine.

The maximum permissible flicker emission according to the Swedish connecting requirement for small energy production units, AMP [3], is $P_{lt} = 0.35$.

In the presence of several turbines, the flicker impact will go down with $\sqrt{N}$ according to [1].

This means that

$$P_{st,tot} = \frac{1}{\sqrt{N}} P_{st,ind} \tag{4.6}$$

where N is the number of turbines.

In Fig. 4.8 the flicker coefficients found for various operating points are presented. It can be mentioned that the official value for this turbine is 2.1, determined by DEWI (A German organization which among other things certify wind turbines), 2.1. Observe that there are also situations where the turbine switches between Δ and Y-connection of the stator, giving some slightly higher values.

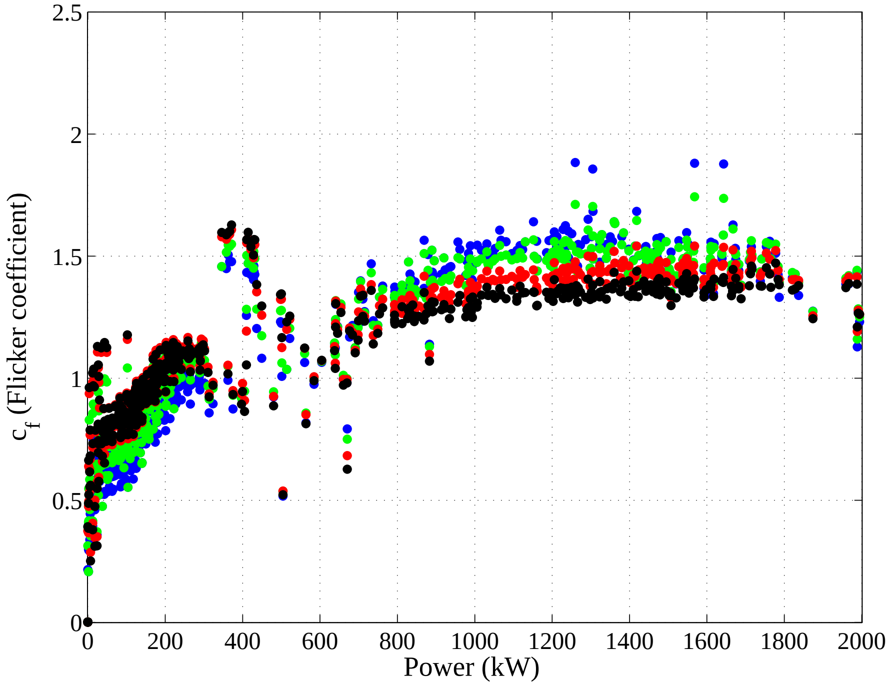

Figure 4.8: Flicker coefficient c_f as a function of produced power for various grid impedance angles. Blue=30 degrees, green=50 degrees, red=70 degrees, black=85 degrees. 10 minute values are presented.

Unfortunately, there were no current and voltage transformers located on the 10 kV side of the transformer. Instead the currents flowing in to the transformer from the 480 V (converter) side as well as from the 690 V (stator) side were summed up. This means that there is a degree of uncertainty in the determination of the flicker coefficient.

The emission levels for the turbine is very low, which makes it almost impossible for this wind turbine to create flicker on any type of grid, the maximum flicker coefficient is around 2. In addition it shall be remembered that the flicker emission goes down with $\sqrt{N}$ where N is the number of turbines.

The flicker emission determination was made using files sampled at 19200

Hz, digitally downsampled to files containing data with 256 Hz data acquisition speed.

4.3 Harmonic current emission

Again, a problem was that there were no transducer mounted on the 10 kV side of the transformer. Instead the voltage on the 690 V side of the transformer was used for the evaluation of the voltage harmonics. The current harmonics were obtained by using the current registered by the stator current and grid side converter current modules.

The Swedish standard EN 50160, [4], states that the voltage total harmonic distortion should be maximum 8 %, which must be said to be a very high value.

Harmonic voltages and currents are always present in the grid. With the introduction of power electronic equipment during the last decades the harmonic levels have risen. [4] states the levels of harmonic voltages that are allowed in the Swedish grid.

A common method to judge the harmonic situation is to form the total harmonic distortion (THD-value).

$$THD_i = \sqrt{\frac{\sum i(n), n > 2}{i(1)_{rated}}} \tag{4.7}$$

and

$$THD_u = \sqrt{\frac{\sum u(n,)n > 2}{u(1)_{rated}}}. \tag{4.8}$$

The harmonic emission was evaluated using files acquired with a data acquisition speed of 19200 Hz. The results are based on 1 seconds data acquisition periods, and the first 100 harmonics have been included in the determination of the THD. In Fig. 4.9 the current THD as a function of produced power is presented.

From the figure the following observations can be made. The current THD is fairly low with a maximum of 2.5 %. In Fig. 4.10 the voltage THD values are presented as a function of produced power. The voltage THD is also well within the limits prescribed by [4] with a maximum value of around 2 %.

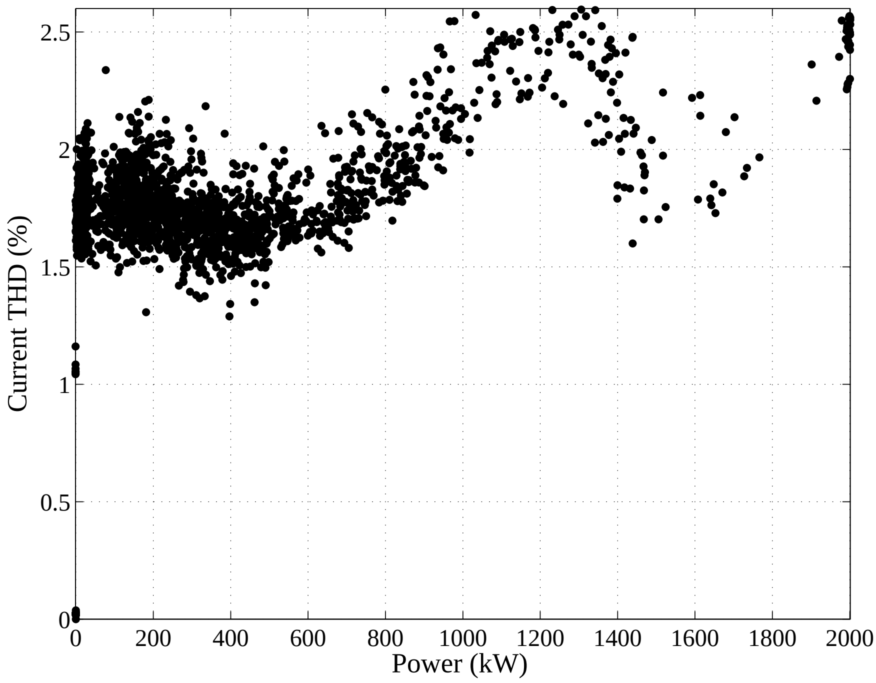

Figure 4.9: Current THD as a function of produced power

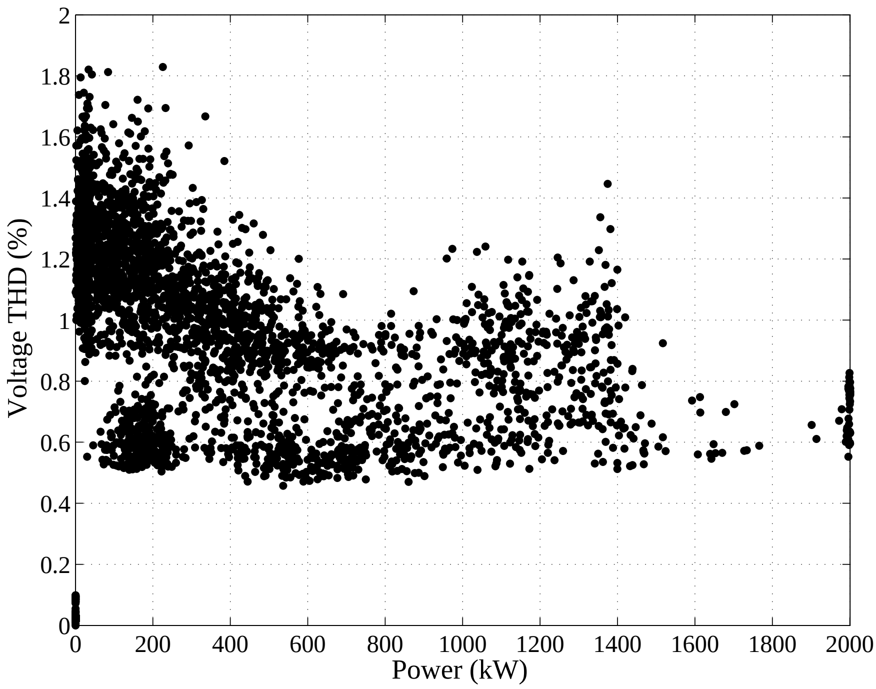

Figure 4.10: Voltage THD as a function of produced power

Chapter 5

Modeling of the DFIG system

In this chapter, the key equations that are needed to assemble a generic model of a DFIG turbine are presented in a fairly compact way. For more details and intermediate steps, the interested reader can consult [7].

5.1 Electric grid connection modeling

The DFIG wind turbine investigated in this work is assumed to be connected to a stiff grid with a voltage of 690 V. The influence of the wind turbine transformer has been neglected. This is because it was not feasible to mount any sensors on the 10 kV side of the transformer. In the turbine studied, all sensors are located on the low-voltage sides of the three-winding transformer, in the DFIG system itself.

5.2 Two-winding representation of electric machines and electric networks

Power system components like the electric network and the generator have three phases in which currents can flow. A possibility is to represent the three-phase system by three simple and separate networks, one single-phase for the zero sequence, and two 2-phase systems for the positive and negative sequence, see [8]. Below follows the transformation for the positive sequence, which is the only sequence that is considered and accounted for in this work.

The α-β transformation transforms the three-phase system in to a two phase system with perpendicular axes, α and β. The α and β axes can be seen also as the real and imaginary axes in a complex plane.

The transformation is given by :

$$\mathbf{v}^s(t) = v_\alpha(t) + jv_\beta(t) = K\left(v_a(t) + e^{j\frac{2\pi}{3}}v_b(t) + e^{-j\frac{2\pi}{3}}v_c(t)\right) \tag{5.1}$$

$$\mathbf{v}^s(t) = K\left(\frac{3}{2}v_a(t) + j\frac{\sqrt{3}}{2}\left(v_b(t) - v_c(t)\right)\right) \tag{5.2}$$

For the **amplitude invariant transformation**, $K = 2/3$, the α-β transformation in (5.2) can be expressed by the matrix form:

$$\begin{bmatrix} v_\alpha(t) \\ v_\beta(t) \end{bmatrix} = \begin{bmatrix} 1 & 0 & 0 \\ 0 & \frac{1}{\sqrt{3}} & -\frac{1}{\sqrt{3}} \end{bmatrix} \begin{bmatrix} v_a(t) \\ v_b(t) \\ v_c(t) \end{bmatrix} \tag{5.3}$$

The inverse two-to-three phase transformation is given by:

$$\begin{bmatrix} v_a(t) \\ v_b(t) \\ v_c(t) \end{bmatrix} = \begin{bmatrix} 1 & 0 \\ -\frac{1}{2} & \frac{\sqrt{3}}{2} \\ -\frac{1}{2} & -\frac{\sqrt{3}}{2} \end{bmatrix} \begin{bmatrix} v_\alpha(t) \\ v_\beta(t) \end{bmatrix} \tag{5.4}$$

5.2.1 Transformation into a rotating reference frame

All the voltage variables just discussed are sinusoidal, with a base frequency of 50 Hz. This complicates the control of the resulting DFIG-system. In order to facilitate the simulation as well as to simplify the control of the system, the mathematical equations can be transformed and solved in a rotating reference system.

Considering the rotating space vector,

$$\mathbf{v}^s(t) = \hat{V}e^{j\omega_k t + \varphi}, \tag{5.5}$$

the following transformation removes the rotation of the vector, making it similar to a standard fixed complex phasor.

$$\mathbf{v}^r(t) = e^{-j\omega_k t}\mathbf{v}^s(t) = \hat{V}e^{j\varphi} \tag{5.6}$$

With this transformation, the space vector is observed from a coordinate system rotating with the angular frequency ω_k.

Considering

$$\mathbf{v}^r(t) = v_x(t) + jv_y(t) \tag{5.7}$$

the definitions of the α-β to x-y transformation and the inverse are

$$\mathbf{v}^r(t) = e^{-j\theta_k(t)}\mathbf{v}^s(t) \tag{5.8}$$

$$\mathbf{v}^s(t) = e^{j\theta_k(t)}\mathbf{v}^r(t) \tag{5.9}$$

where

$$\theta_k(t) = \int \omega_k dt. \tag{5.10}$$

In matrix form, the transformation becomes:

$$\begin{bmatrix} v_x(t) \\ v_y(t) \end{bmatrix} = \begin{bmatrix} cos(\theta_k(t)) & sin(\theta_k(t)) \\ -sin(\theta_k(t)) & cos(\theta_k(t)) \end{bmatrix} \begin{bmatrix} v_\alpha(t) \\ v_\beta(t) \end{bmatrix} \tag{5.11}$$

$$\begin{bmatrix} v_\alpha(t) \\ v_\beta(t) \end{bmatrix} = \begin{bmatrix} cos(\theta_k(t)) & -sin(\theta_k(t)) \\ sin(\theta_k(t)) & cos(\theta_k(t)) \end{bmatrix} \begin{bmatrix} v_x(t) \\ v_y(t) \end{bmatrix} \tag{5.12}$$

In order to transform a three-phase system into a x-y space-vector, the quantities must be transformed first to the α-β system and then from α-β to x-y.

5.2.2 Symmetrical components

In the ideal (symmetrical) case, the magnitudes of all phases are equal and separated from each other by exactly 120 degrees. It then follows that the sum of the instantaneous values of the voltages and currents are zero.

However, during both steady state and faults, the phase voltages may be asymmetrical. They can be expressed into zero (V_0), positive (V_+) and negative sequence(V_-) components. A description of the decomposition of the quantities can be found in [8].

In Fig. 5.1 the components making up an unsymmetrical signal are presented.

Since the wind turbine transformer has a Δ-connection towards the 10 kV side and a mid-point grounded Y-connection on the low-voltage side, there can be no zero-sequence components subjected to the DFIG system. Therefore, there is no need in this study to model the zero sequence component. If the power system, disturbances influencing the turbine are symmetrical, it is sufficient to only use the positive sequence component.

In the simulations made in this report, the focus is to make the system remain connected. Only the positive sequence components has been

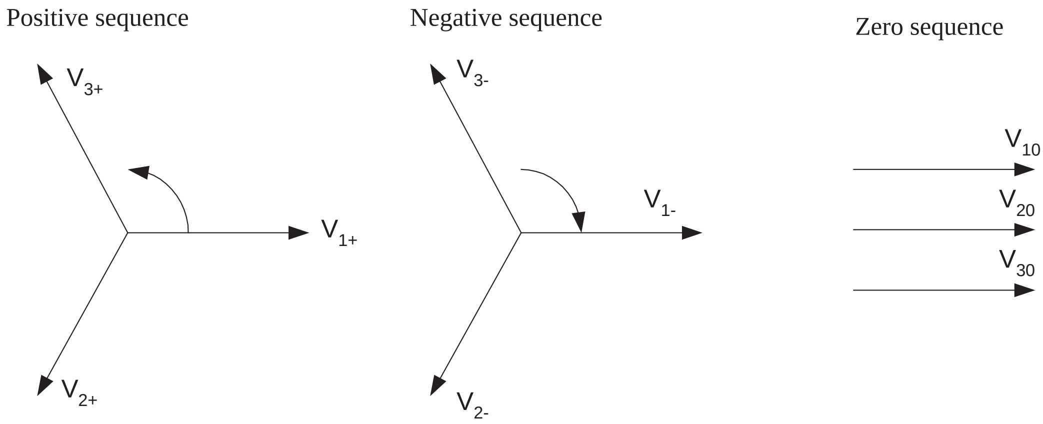

Figure 5.1: Symmetrical components. Observe that the three voltage magnitudes in the three systems all have the same magnitudes.

"treated", i.e. no negative sequence current controller has been used nor has the negative sequence in the voltage been handled.

. There is no major point in maintaining a symmetrical waveform during the power system disturbance, so it is not necessary to control the negative sequence currents to zero. Therefore, only the positive sequence component is controlled.

5.3 Field orientation

In order to construct a high-performance controller for the DFIG system, the equations must be oriented in such a way that the dominating 50Hz-components of electric variables (currents, voltages, and fluxes) can be easily controlled.

This is done by formulating the state equations in a rotating coordinate frame. It is common to align the rotating frame with the rotor flux, stator flux or the stator voltage, and such a system is commonly referred to as a dq-system. Research has shown [6] that an alignment of the imaginary axis of the rotating frame with the stator voltage gives the highest degree of stability.

The angle which is needed to transform the 50 Hz system into a rotating coordinate frame with the imaginary axis aligned with the q-direction is of course unknown. The methodology used to obtain the xy-system cannot be directly used. Instead of using $\theta = t\omega_k$ the transformation angle must be found from one of the fluxes, which for the DFIG-system commonly is the stator flux:

$$\angle\Psi_s(t) = atan(\frac{\Psi_{sq}(t)}{\Psi_{sd}(t)}) \tag{5.13}$$

or from the applied voltage, i.e

$$\theta(t) = atan(\frac{u_{sq}(t)}{u_{sd}(t)}) + \frac{\pi}{2}. \tag{5.14}$$

Then the following transformation can be used for this purpose,

$$\begin{bmatrix} u_d(t) \\ u_q(t) \end{bmatrix} = \begin{bmatrix} cos(\theta(t)) & sin(\theta(t)) \\ -sin(\theta(t)) & cos(\theta(t)) \end{bmatrix} \begin{bmatrix} u_\alpha(t) \\ u_\beta(t) \end{bmatrix}$$

A problem with the direct determination method presented above is that any disturbances in the voltage will also directly affect θ. In order to have a more stable determination, a good choice is to use a phase-locked loop (PLL) which in principle functions as a low-pass filter. In this work the following PLL-structure has been used:

$$\frac{\hat{w_g}(t)}{dt} = k_i(\theta(t) - \hat{\theta}(t)) \tag{5.15}$$

$$\frac{\hat{\theta}(t)}{dt} = \hat{w_g}(t) + k_p(\theta(t) - \hat{\theta}(t)) \tag{5.16}$$

5.4 Induction machine model in the synchronously rotating reference frame

5.4.1 DFIG Dynamic Model

In the following development, the time argument "(t)" will be excluded for simplicity.

Electrical Dynamics

The equations that govern the stator and rotor dynamics are respectively:

$$\mathbf{v}_s^s = -R_s\mathbf{i}_s^s - \frac{d\mathbf{\Psi}_s^s}{dt} \tag{5.17}$$

$$\mathbf{v}_r^r = -R_r\mathbf{i}_r^r - \frac{d\mathbf{\Psi}_r^r}{dt} \tag{5.18}$$

where	$\mathbf{v}_s^s$	is the stator voltage space vector;
	R_s	is the resistance of the stator winding;
	$\mathbf{i}_s^s$	is the stator current space vector;
	$\mathbf{\Psi}_s^s$	is the stator flux linkage space vector;
	$\mathbf{v}_r^r$	is the stator voltage space vector;
	R_r	is the resistance of the rotor winding; and
	$\mathbf{i}_r^r$	is the rotor current space vector;
	$\mathbf{\Psi}_r^r$	is the rotor flux linkage space vector;

It should be pointed out that this model is purely mathematical. To be studied, the real stator currents must first be transformed back to the stationary reference system using (5.9) and then use the two–phase to three-phase transformation (5.4).

The physical rotor quantities present an additional complication. The rotor variables have to be transformed into the "rotor system" which means that, in addition to the transformations mentioned above, a transformation must first be done from the rotor coordinate system into the synchronously rotating coordinate frame. To perform this operation, knowledge of the rotor position is needed. This requires a good tracking of the rotor position. The following equation is used:

$$\theta_r = \int \omega_r dt \tag{5.19}$$

and the rotor space vectors become

$$\mathbf{v}_r^s = e^{j\theta_r}\mathbf{v}_r^r \tag{5.20}$$

$$\mathbf{i}_r^s = e^{j\theta_r}\mathbf{i}_r^r \tag{5.21}$$

$$\mathbf{\Psi}_r^s = e^{j\theta_r}\mathbf{\Psi}_r^r. \tag{5.22}$$

Substituting (5.20), (5.21) and (5.22) in (5.18), the electrical equations of the stator and rotor become

$$\mathbf{v}_s^s = -R_s\mathbf{i}_s^s - \frac{d\mathbf{\Psi}_s^s}{dt} \tag{5.23}$$

$$\mathbf{v}_r^s = -R_r\mathbf{i}_r^s - \frac{d\mathbf{\Psi}_r^s}{dt} + j\omega_r\mathbf{\Psi}_r^s \tag{5.24}$$

In order to transform the quantities to an arbitrary rotating frame of speed ω_k the $\alpha\beta - xy$ transformation is required.

Applying the relation in (5.8) to (5.23) and (5.24), the electrical equation of the stator and rotor become

$$\mathbf{v}_s^k = -R_s\mathbf{i}_s^k - j\omega_k\mathbf{\Psi}_s^k - \frac{d\mathbf{\Psi}_s^k}{dt} \tag{5.25}$$

and

$$\mathbf{v}_r^k = -R_r\mathbf{i}_r^k + j(\omega_r - \omega_k)\mathbf{\Psi}_r^k - \frac{d\mathbf{\Psi}_r^k}{dt}. \tag{5.26}$$

When the dynamic electrical circuit diagram and the state-space model of the system are derived, it is necessary to substitute the fluxes in (5.25) and (5.26), by their respective currents and inductances.

The relation between the stator and rotor flux linkages is given by the air gap flux Ψ_a^k, expressed by

$$\mathbf{\Psi}_a^k = L_m\mathbf{i}_m^k \tag{5.27}$$

where L_m is the mutual inductance between the stator and the rotor; and
$\mathbf{i}_m^k$ is the magnetizing current equivalent to

$$\mathbf{i}_m^k = \mathbf{i}_s^k + \mathbf{i}_r^k \tag{5.28}$$

The stator flux is equivalent to the sum of the airgap flux and the stator leakage flux. The same relation is valid for the rotor flux. Therefore

$$\mathbf{\Psi}_s^k = L_m\mathbf{i}_m^k + L_{sl}\mathbf{i}_s^k \tag{5.29}$$

$$\mathbf{\Psi}_r^k = L_m\mathbf{i}_m^k + L_{rl}\mathbf{i}_r^k \tag{5.30}$$

Rewriting (5.25) and (5.26), but using the relations (5.29) and (5.30), the electrical equation of the stator and rotor becomes

$$\mathbf{v}_s^k = -R_s\mathbf{i}_s^k - j\omega_k\mathbf{\Psi}_s^k - L_{sl}\frac{d}{dt}\mathbf{i}_s^k - L_m\frac{d}{dt}\mathbf{i}_m^k \tag{5.31}$$

$$\mathbf{v}_r^k = -R_r \mathbf{i}_r^k + j(\omega_r - \omega_k)\mathbf{\Psi}_r^k - L_{rl}\frac{d}{dt}\mathbf{i}_r^k - L_m \frac{d}{dt}\mathbf{i}_m^k \tag{5.32}$$

From (5.31) and (5.32), it is possible to derive the electrical equivalent circuit of the open rotor induction machine.

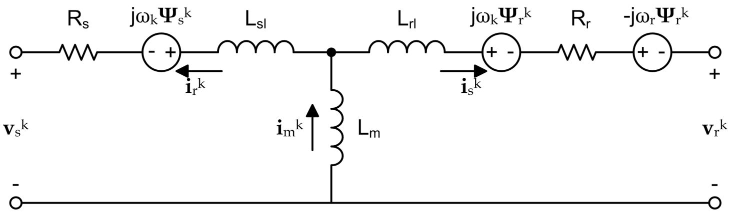

Figure 5.2: Electrical equivalent circuit

This circuit is similar to the T-equivalent circuit of short-circuited rotor induction machines or Park equivalent model [5].

Defining

$$L_s = L_m + L_{sl} \tag{5.33}$$

$$L_r = L_m + L_{rl} \tag{5.34}$$

and substituting all fluxes in (5.31) and (5.32) by their equivalent inductances and currents, the electrical equation of the stator and rotor becomes

$$\mathbf{v}_s^k = -R_s \mathbf{i}_s^k - j\omega_k L_s \mathbf{i}_s^k - j\omega_k L_m \mathbf{i}_r^k - L_s \frac{d}{dt}\mathbf{i}_s^k - L_m \frac{d}{dt}\mathbf{i}_r^k \tag{5.35}$$

and

$$\mathbf{v}_r^k = -R_r \mathbf{i}_r^k - j(\omega_k - \omega_r)L_r \mathbf{i}_r^k - j(\omega_k - \omega_r)L_m \mathbf{i}_s^k - L_r \frac{d}{dt}\mathbf{i}_r^k - L_m \frac{d}{dt}\mathbf{i}_s^k. \tag{5.36}$$

Separating the quantities in (5.35) and (5.36) into their real and imaginary parts and putting them into matrix form the electrical equations become:

$$\mathbf{V} = \mathbf{RI} + \mathbf{L}\dot{\mathbf{I}} \tag{5.37}$$

$$\begin{bmatrix} v_{sx}^k \\ v_{sy}^k \\ v_{rx}^k \\ v_{ry}^k \end{bmatrix} = \begin{bmatrix} -R_s & \omega_k L_s & 0 & \omega_k L_m \\ -\omega_k L_s & -R_s & -\omega_k L_m & 0 \\ 0 & (\omega_k - \omega_r)L_m & -R_r & (\omega_k - \omega_r)L_r \\ -(\omega_k - \omega_r)L_m & 0 & -(\omega_k - \omega_r)L_r & -R_r \end{bmatrix} \begin{bmatrix} i_{sx}^k \\ i_{sy}^k \\ i_{rx}^k \\ i_{ry}^k \end{bmatrix}$$

$$+ \begin{bmatrix} -L_s & 0 & -L_m & 0 \\ 0 & -L_s & 0 & -L_m \\ -L_m & 0 & -L_r & 0 \\ 0 & -L_m & 0 & -L_r \end{bmatrix} \frac{d}{dt} \begin{bmatrix} i_{sx}^k \\ i_{sy}^k \\ i_{rx}^k \\ i_{ry}^k \end{bmatrix} \qquad (5.38)$$

The state-space system has the structure

$$\dot{\mathbf{I}} = \mathbf{AI} + \mathbf{BV} \qquad (5.39)$$

where $\mathbf{I}$ is the state's matrix; and
$\mathbf{V}$ is the input's vector

Transforming (5.38) in the form described by (5.39), leads to

$$\begin{aligned} \mathbf{A} &= \mathbf{L^{-1}R} \\ \mathbf{B} &= \mathbf{L^{-1}} \end{aligned}$$

Mechanical Dynamics

The mechanical dynamics of the machine are described by

$$J\frac{d}{dt}\omega_{mech} = T_e - T_l. \qquad (5.40)$$

The active power is found, using amplitude invariant transformation (k=2/3), to be:

$$\begin{aligned} P_e &= \frac{3}{2} Re\left\{\mathbf{v}^k \mathbf{i}^{k*}\right\} \qquad (5.41) \\ &= \frac{3}{2}\left(v_x^k i_x^k + v_y^k i_y^k\right) \end{aligned}$$

The Γ Model

In order to simplify the controller design, it is possible to modify the induction machine equations slightly by "moving" the placement of the magnetizing inductance. The procedure for this is omitted here, but can be found in [7]. The resulting equivalent circuit is presented in Fig. 5.3. Observe that the reference notation that has been chosen in this work is that all currents flow out of the machine. The equivalent Γ model has the following circuit

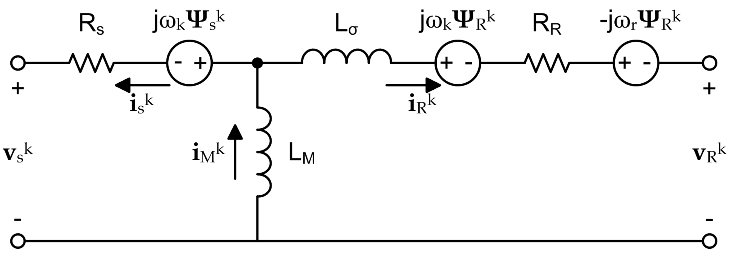

Figure 5.3: Electrical equivalent circuit - Γ model

The equivalent Γ parameters can be found in [7]. Some of them are described below:

$$\mathbf{b} = \frac{\mathbf{L_s}}{\mathbf{L_M}} \tag{5.42}$$

$$\mathbf{L_M} = \mathbf{L_s} \tag{5.43}$$

$$\mathbf{L}_\sigma = \mathbf{L_r}\left(\frac{\mathbf{L_s}}{\mathbf{L_m}}\right)^{\mathbf{2}} - \mathbf{L_s} \tag{5.44}$$

This is the same as [9], where L_σ is given by:

$$\mathbf{L}_\sigma = \mathbf{b}\mathbf{L_{sl}} + \mathbf{b^2}\mathbf{L_{rl}} \tag{5.45}$$

and R_R is given by

$$\mathbf{R_R} = \mathbf{b^2}\mathbf{R_r} \tag{5.46}$$

The Γ-equivalent model quantities relate to the T-equivalent model quantities as follows:

$$\mathbf{v_R} = b\mathbf{v_r} \tag{5.47}$$

$$\mathbf{i_R} = \frac{\mathbf{i_r}}{b} \tag{5.48}$$

5.5 Modeling of the DC-link

The DC-link voltage is determined from the current that flows into the DC-link from the rotor, and the current that flows out of the DC-link to the grid.

$$C\frac{dv_{dc}}{dt} = i_{dcfromrotor} - i_{dctowardsgridconverter} \tag{5.49}$$

When DC-link the voltage exceeds a certain limit, the DC-link crowbar is activated. During this time, the current

$$i_{crowbar} = \frac{v_{dc}}{R} \tag{5.50}$$

flows through the braking resistor.

This means that the equation for the DC-link current is rewritten as:

$$C\frac{dv_{dc}}{dt} = i_{dcfromrotor} - i_{dctowardsgridconverter} - i_{crowbar} \tag{5.51}$$

The currents $i_{dcfromrotor}$ and $i_{dctowardsgridconverter}$ can be determined from the active power flowing from the rotor and to the grid, according to

$$\frac{3}{2}Re\left(\mathbf{v_r}\mathbf{i_r}^*\right) = v_{dc}i_{dcfromrotor} \tag{5.52}$$

$$\frac{3}{2}Re\left(\mathbf{v_g}\mathbf{i_g}^*\right) = v_{dc}i_{dctowardsgridconverter} \tag{5.53}$$

In Fig. 5.4 a photograph of the DC-crowbar resistors is shown.

As a final protection for the rotor, it is possible to short-circuit the rotor windings directly, as was shown in Fig. 3.2. This can be implemented using a three-phase diode rectifier bridge connected to an IGBT (Insulated gate bipolar transistor) on the dc-side of the diode bridge. Although it is designed to handle the protection of a 2 MW wind turbine, it is actually very small in size, as can be noted in Fig. 5.5 where a photograph of the AC-crowbar is shown. Observe that in this crowbar, no resistances are used, since the currents anyway will be limited by the rotor resistance and rotor leakage inductance.

5.6 Parameters for the generic DFIG system

The parameters of the generator are taken from an old fixed-speed 2 MW Bonus machine [7].

Figure 5.4: DC crowbar resistor with a current sensor (blue).

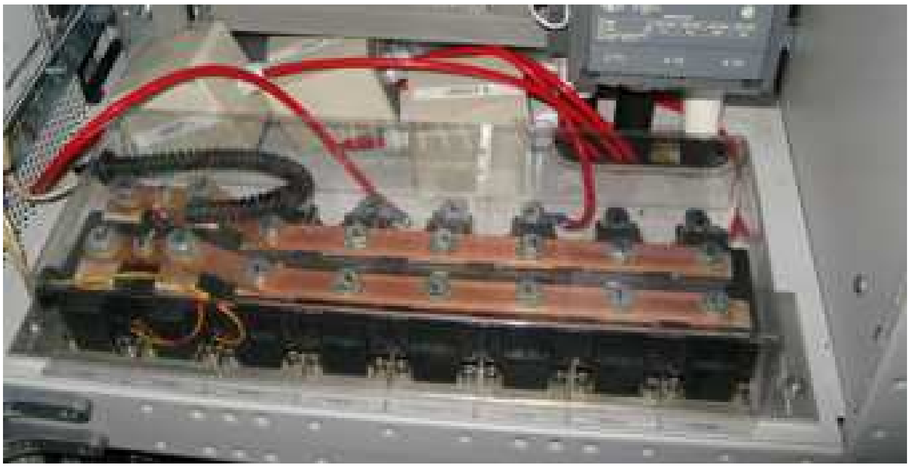

Figure 5.5: AC crowbar circuit with the purpose of protecting the rotor windings.

stator resistance	R_s	$2.2m\Omega$
rotor resistance	R_r	$1.8m\Omega$
stator leakage inductance	$L_{s\lambda}$	$0.12mH$
rotor leakage inductance	$L_{r\lambda}$	$0.05mH$
magnetizing inductance	L_m	$2.9mH$
machine and rotor inertia	J	$460kgm^2$
synchronous speed	n_s	$1500rpm$
gear-box ratio		113.5

The grid filter inductance is assumed to be 5 % giving $L_f = 2mH$. The filter resistance R_f is assumed to be $1m\Omega$. The DC-link capacitor value is assumed to be equal to that of an ordinary industrial drive and is set to $C = 30mF$. The DC-link nominal voltage has been set to 800 V with the dc crowbar activation limit set to 950 V. The braking resistor R value is assumed to be 0.13Ω.

Chapter 6

Control of the DFIG system

As mentioned before, the control of the DFIG-system will be done in a rotating reference frame aligned to the stator voltage. This is also the voltage that is applied to the grid side converter and its filter.

The scope of study for this project has been the behavior of the system during power system disturbances. In particular, it was desired to verify that the turbine does not disconnect from the grid due to voltage dips over a certain time-voltage limit. Svenska Kraftnät (SvK) has stated an undervoltage immunity limit which wind parks should be able to ride through without disconnecting. This immunity dip is presented in Fig. 6.1, dashed curve represents the limit for a large wind park and solid for a smaller wind park.

It is worth mentioning is that most voltage disturbances are about 100 ms, shorter than the dip durations specified in Fig. 6.1. Only such short dips were recorded during the measurement period of this project.

The DFIG system, marked with the sensor signals that are used for the controller, is depicted in Fig. 6.2. The active and reactive powers are formed using (7.1) and (7.2).

A positive direction of current is defined as when the currents flow out from the generator, i.e towards the grid.

No speed control of the turbine has been implemented. The events have been so short that it was considered to be acceptable to only control the torque.

6.1 Rotor current controller

The rotor current controller used in this work is

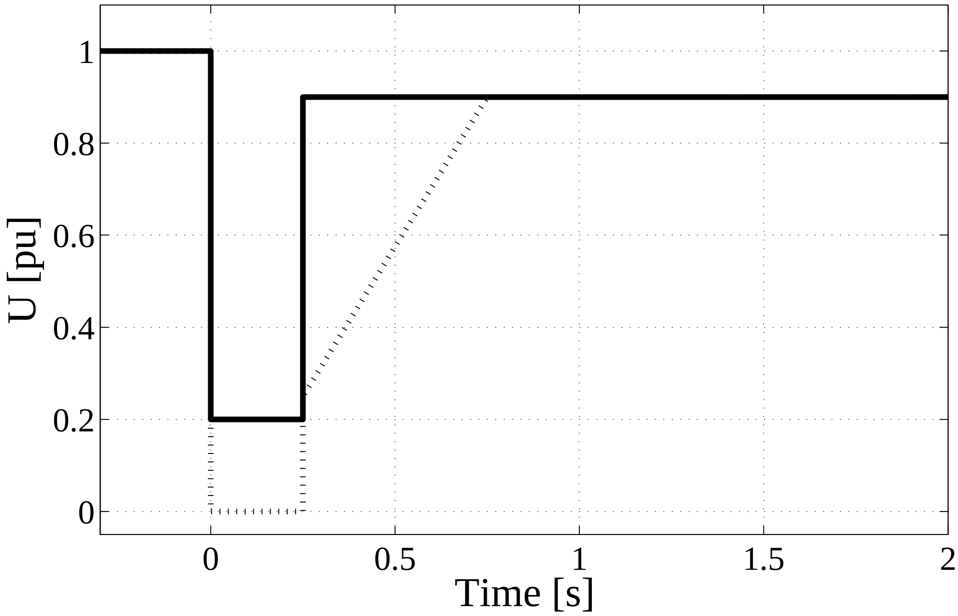

Figure 6.1: Undervoltage immunity capability curve from the Swedish transmission system operator SvK. Dashed for a larger wind park and solid for a smaller wind park.

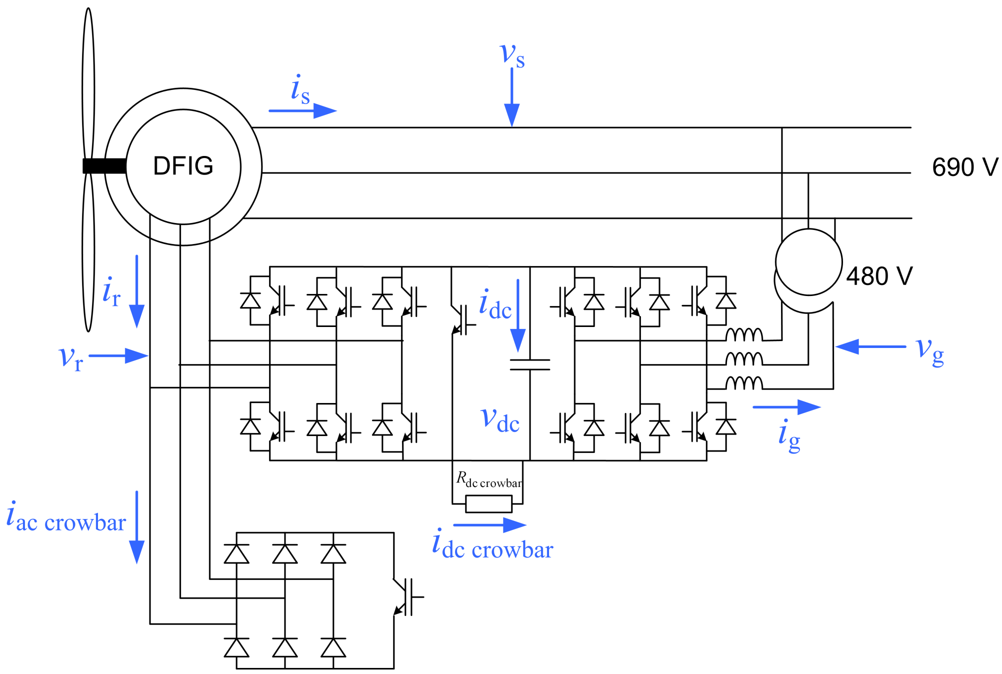

Figure 6.2: DFIG system marked with the signals used for the controllers, and indication of the direction of the currents.

$$v_{Rd} = k_{p_{rcc}}(i_{Rd}^{ref} - i_{Rd}) - \omega_2 L_\sigma i_{Rq} + v_{sdLP} - (\frac{R_s}{L_M}\Psi_{sdLP}) + \omega_r \Psi_{sqLP} \quad (6.1)$$
$$v_{Rq} = k_{p_{rcc}}(i_{Rq}^{ref} - i_{Rq}) + \omega_2 L_\sigma i_{Rd} + v_{sqLP} - (\frac{R_s}{L_M}\Psi_{sqLP}) - \omega_r \Psi_{sdLP}$$

where

$$v_{sdLP} = \frac{\alpha_{ac}}{s + \alpha_{ac}} v_{sd} \quad (6.2)$$

$$v_{sqLP} = \frac{\alpha_{ac}}{s + \alpha_{ac}} v_{sq} \quad (6.3)$$

$$\Psi_{sdLP} = \frac{\alpha_{aco}}{s + \alpha_{aco}} \Psi_{sd} \quad (6.4)$$

$$\Psi_{sqLP} = \frac{\alpha_{aco}}{s + \alpha_{aco}} \Psi_{sq} \quad (6.5)$$

and ω_2 is the slip frequency given by:

$$\omega_2 = \omega_s - \omega_r = s\omega_s \quad (6.6)$$

The rotor current controller achieves reference currents generated by an outer reactive power controller and an outer torque reference value. Where necessary, these outer references are already based on integrals of error. Thus, there is no integrator in the rotor current controller.

The Γ-equivalent model quantities relate to the T-equivalent model quantities as stated in Section 5.4.1.

The proportional part of the rotor current controller is:

$$k_{p_{rcc}} = \alpha_{rcc} L_\sigma. \quad (6.7)$$

6.2 Grid current controller

Neglecting any losses in the grid filter, the equations that govern the grid current controller in the stator flux oriented rotating reference frame (dq-system), are given by [10],

$$v_{gd} = k_{p_{gcc}}(i_{gd}^{ref} - i_{gd}) - \omega_s L_f i_{gq} + n_{ratio} v_{sd} \quad (6.8)$$
$$v_{gq} = k_{p_{gcc}}(i_{gq}^{ref} - i_{gq}) + \omega_s L_f i_{gd} + n_{ratio} v_{sq}$$

where n_{ratio} is the ratio of the transformer present in Figure 6.2

$$n_{ratio} = \frac{0.48}{0.69} \tag{6.9}$$

The proportional part of the grid current controller is determined using internal model control (IMC) and is given by

$$k_{p_{gcc}} = \alpha_{gcc} L_f. \tag{6.10}$$

Again, the integrator part has been omitted.

6.3 Power Controllers

The active power is controlled through the electrodynamical torque

$$T_e^{ref} = \frac{3}{2}\frac{P_e^{ref}}{\omega_r}. \tag{6.11}$$

The electrodynamical torque can be written in several ways involving fluxes and currents. Denoting with the superscript '$*$' the conjugate of the complex number, a convenient notation for the DFIG system is

$$T_e = \frac{3}{2}\mathrm{Im}(\mathbf{\Psi_s}\mathbf{i_R}^*) \tag{6.12}$$

which, with the flux oriented completely in the d-direction, gives

$$T_e = \frac{3}{2}\mathrm{Im}(\Psi_{sd} i_{Rq}) \tag{6.13}$$

From (6.11) the reference value for quadrature component of the rotor current can be found to be:

$$i_{Rq}{}^{ref} = \frac{2}{3}\frac{T_e{}^{ref}}{\Psi_{sd}} \tag{6.14}$$

The reactive power can be generated in two ways in the DFIG system: from the stator, by feeding reactive current into the rotor and from the grid side converter. In this work only the first option has been considered. The relation between the reactive current fed into the rotor and the reactive power coming out of the stator is (neglecting the derivative of the stator flux):

$$Q_s = \frac{3}{2}\omega_s \mathbf{\Psi_s} i_{sd} = \frac{3}{2}\omega_s(\frac{\Psi_s}{L_M} - i_{Rd}) \tag{6.15}$$

In [7] the following reactive rotor current controller is suggested:

$$
{i_{Rd}}^{ref} = k_{iQ} \int \left({Q_s}^{ref} - Q_s \right) dt - \frac{\alpha_{rpc}}{R_s} \left(1 - \frac{\alpha_{co}}{s + \alpha_{co}} \right) \Psi_{sd} \tag{6.16}
$$

where the selection

$$
k_{iQ} = -\frac{2\alpha_{rpc}}{3V_{phase}} \tag{6.17}
$$

can be made. In this work, α_{rpc} and α_{co} are here set to 10 and 6.28 rad/sec respectively.

6.4 DC-link controller

It is more convenient to control the energy stored in the DC-link capacitor, instead of its voltage. In [11], the following reference value for active component for the grid converter current is suggested

$$
P^{ref} = k_{p_{dc}} \frac{\left({v_{dc}}^{ref} \right)^2 - v_{dc}^2}{2} - H_{dc}(p) P_r \tag{6.18}
$$

$$
k_{p_{dc}} = \alpha_{dc} C_{dc} \tag{6.19}
$$

$$
\alpha_{dc} \leq 0.1 \alpha_{gcc} \tag{6.20}
$$

$$
{i_{gq}}^{ref} = \frac{P^{ref}}{H_{dc}(p) \left| \mathbf{v_g} \right|} \tag{6.21}
$$

$$
H_{dc}(s) = \frac{\alpha_{dc}}{s + \alpha_{dc}} \tag{6.22}
$$

It is possible to also use a small integrating term. It has been decided to use only a proportional part, since the feedforward term of (6.18) anyway brings the voltage fairly close to its reference value.

Chapter 7

Description of the measurement system

The measurement period was from May 2008 to December 2008. In Fig. 7.1 the locations of the installed sensors of the measurement system are depicted.

The voltages are measured using LEM AV 100-1000 modules. The mounting of the 6 modules measuring the rotor voltages and the voltage on the AC side of the grid converter (on the other side of the filter) can be noted from the photograph of Fig. 7.2.

The stator currents are measured using the current sensor LEM LT4000-S which can handle peak currents of more than 5 kA, in the case a short-circuit occurs very close to the turbine would occur. Still, these sensors are mounted in such a way that they only measure half of the stator current. Most other currents are measured using LEM LT505-S modules, which can measure a peak current of 1200 A. The mounting for the currents coming out of the grid side converter after the grid filter can be seen in Fig. 7.3

The rotor currents were measured using the LEM module PR2000. Also here only half of each phase current was measured. The mounting can be observed in Fig. 7.4

In Fig. 7.5 the complete set-up of all modules used in the installation is shown.

In Fig. 7.6 the arrangement of the acquisition computer as well as the signal conditioning box is presented. In the photograph, we are looking toward the rear of the nacelle. The generator is located to the left, and the converter is located to the right.

A remote connection makes it possible to confirm proper operation of the system, change the acquisition set-up, and transfer measurement results to the office from the turbine. In Fig. 7.7 an example is shown of the ”monitor display” presented to a viewer using the system.

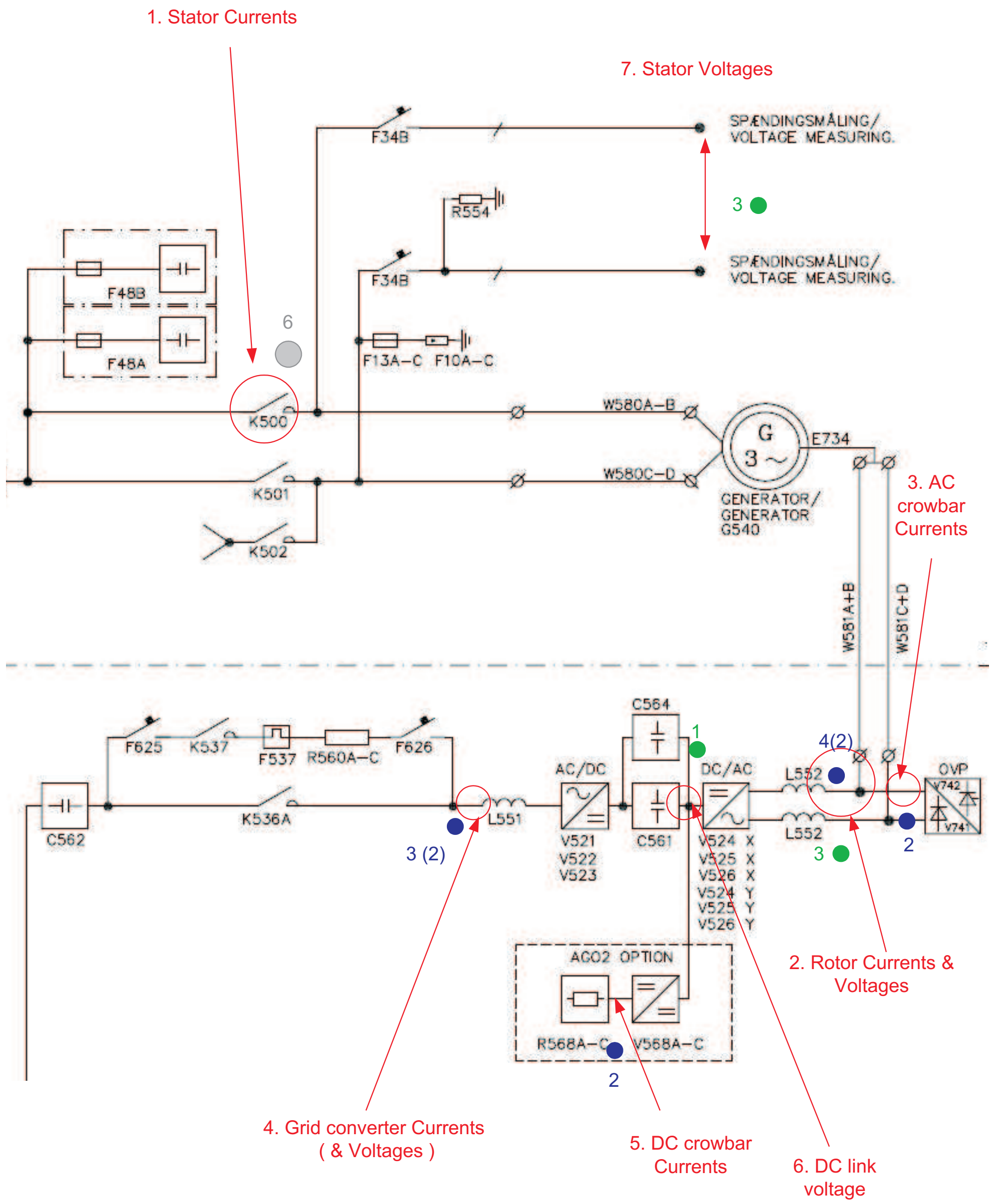

Figure 7.1: Location of current voltage sensors.

Figure 7.2: Voltage sensors measuring the voltages on the rotor as well as on the 480 V side of the wind turbine transformer.

Figure 7.3: Grid converter current measurement.

Figure 7.4: Rotor current measurement.

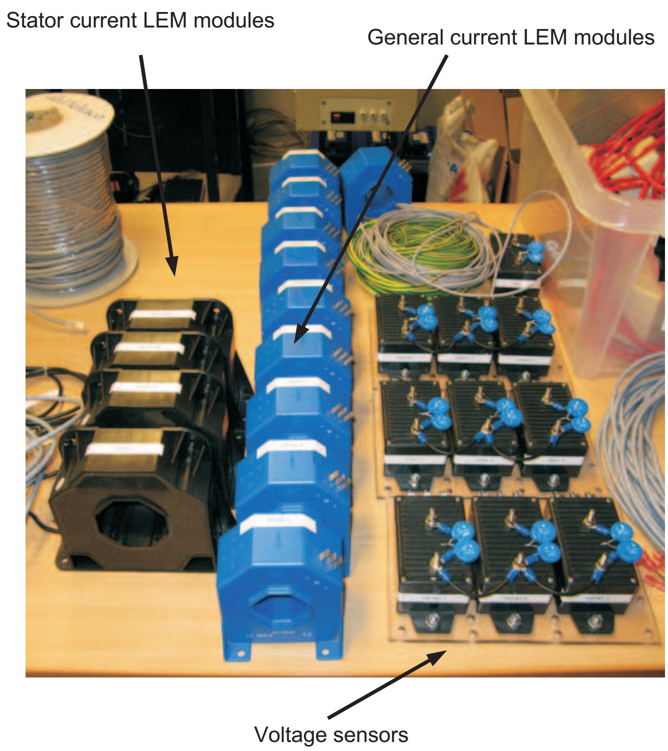

Figure 7.5: Voltage and current sensors used.

Figure 7.6: Physical arrangement of the signal conditioning box and data acquisition computer, at the rear of the nacelle.

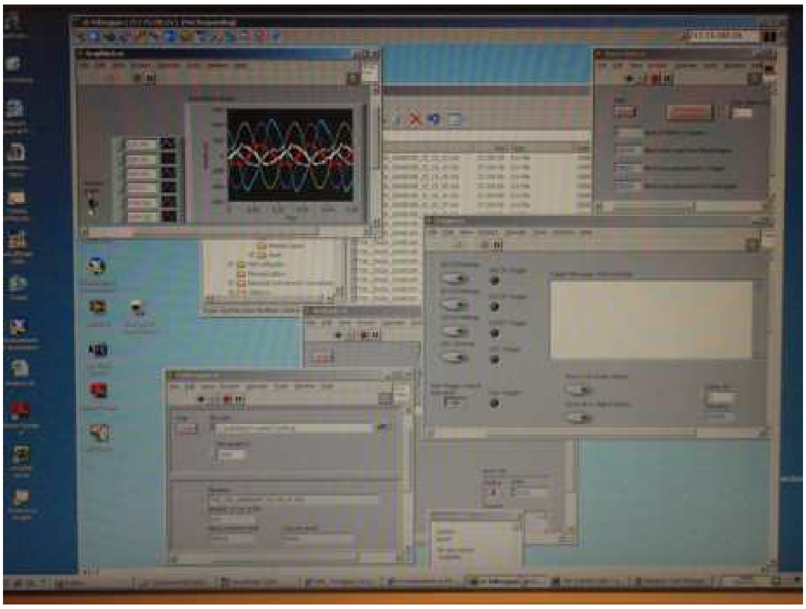

Figure 7.7: The view on the computer screen, also accessible remotely from the office.

In total 24 channels were stored with a sampling rate of 256 Hz, down-sampled from a raw sampling of 19200 Hz. A trigger operating on several of the signals was constructed using the software LabView. When it initiated, a 20 second file with a sampling rate of 19200 Hz was acquired showing 10 seconds before and 10 seconds after the event.

The signals from each transducer pass through a signal conditioning box, where they are transformed to voltages in the range of +- 5 V. These signals are then in turn fed into the DAQ card located in the data acquisition computer where they are filtered and then sampled simultaneously using 24 parallel individual A/D-converters. Finally, the active power is formed from the measured current and voltages according to

$$P = u_1 i_1 + u_2 i_2 + u_3 i_3 \tag{7.1}$$

and the reactive power is formed according to

$$Q = \frac{1}{\sqrt{3}}(u_2 - u_3)i_1 + (u_3 - u_1)i_2 + (u_1 - u_2)i_3. \tag{7.2}$$

Chapter 8

Simulated behavior during disturbances

8.1 Response to an ideal synthetic voltage dip

In Fig. 8.1 the voltages during an ideal voltage dip used for the simulations in this section are presented.

The wind turbine is producing about 1.2 MW when the dip comes. The resulting active and reactive powers from the stator, rotor and converter are presented in Figs. 8.2, 8.3 and 8.4. It can be noted that although the rotor active power is very large, the grid converter manages to keep the apparent power within a reasonable 600 kVA limit. The focus was on making a robust controller that keeps the turbine on-line is evident from the figures- once the dip is recovered; it takes a while before the turbine is back to its initial operating condition.

Due to the very large rotor power peaks, and the limited power transfer capability of the grid side converter, the crowbar has to act to drain energy from the DC-link, which can be noted in Fig. 8.5 which presents the DC-link crowbar current. The resulting DC-link voltage is presented in Fig. 8.6

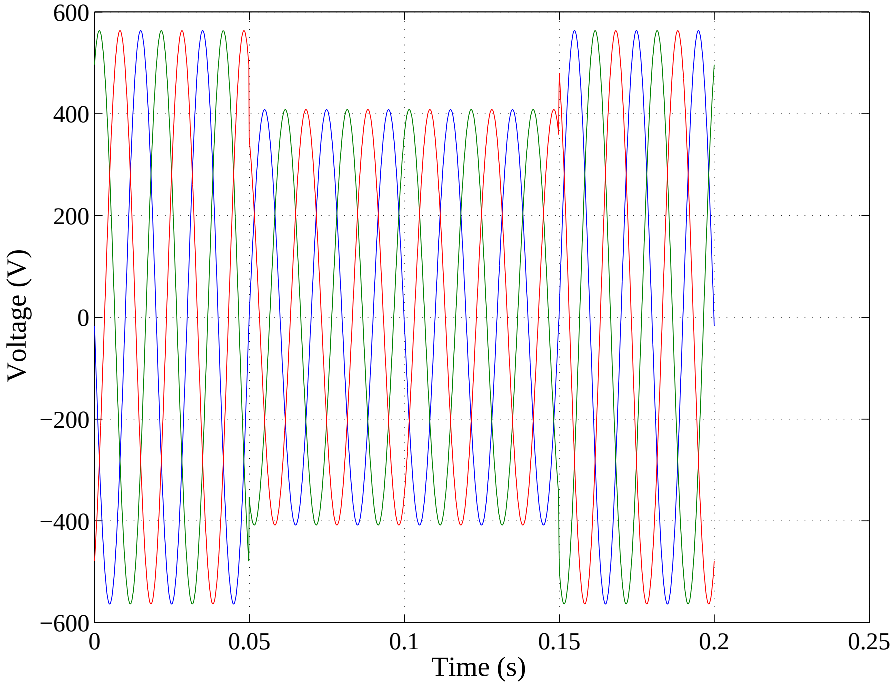

Figure 8.1: Synthetic voltage dip.

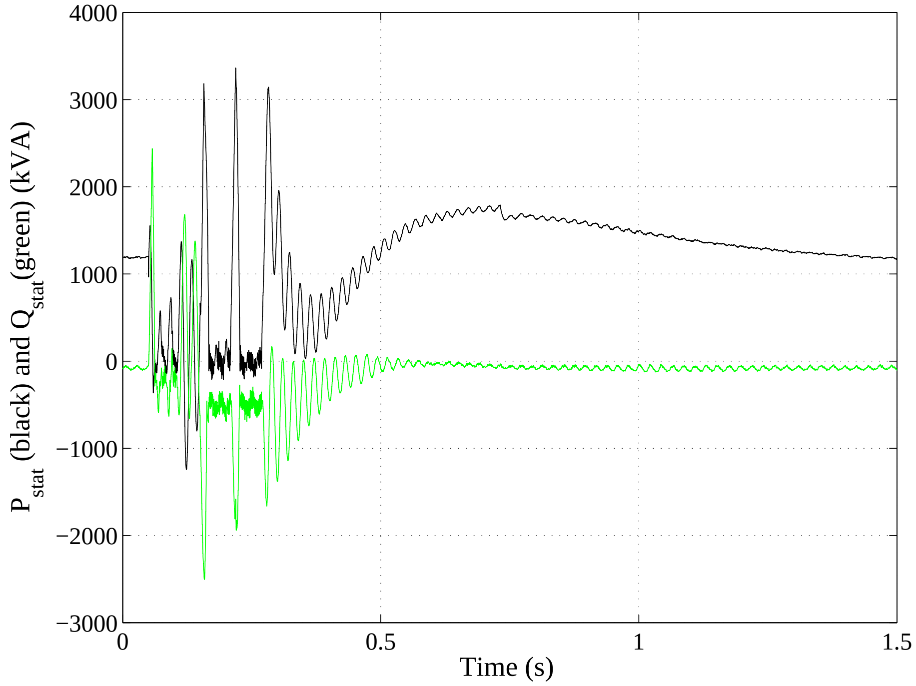

Figure 8.2: Active and reactive power from the stator during the synthetic voltage dip.

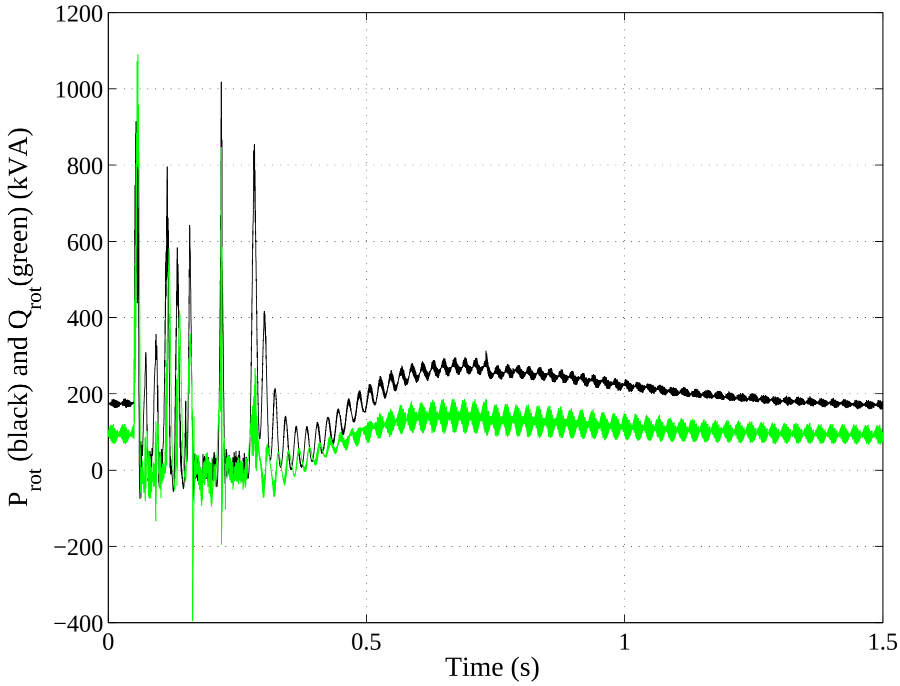

Figure 8.3: Active and reactive power from the rotor during the synthetic voltage dip.

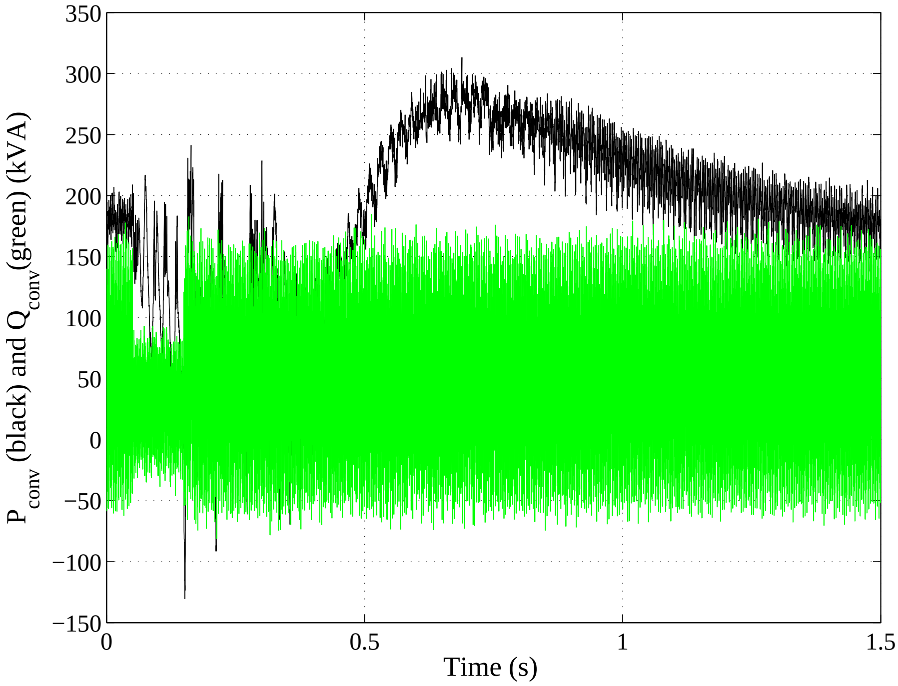

Figure 8.4: Active and reactive power from the grid side converter during the synthetic voltage dip.

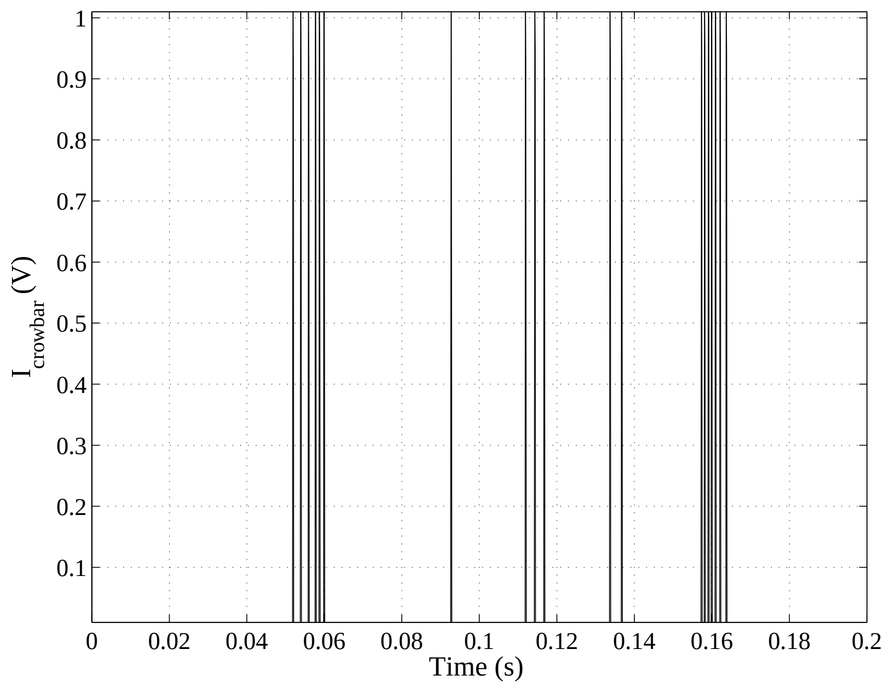

Figure 8.5: DC-link crowbar current during the synthetic voltage dip.

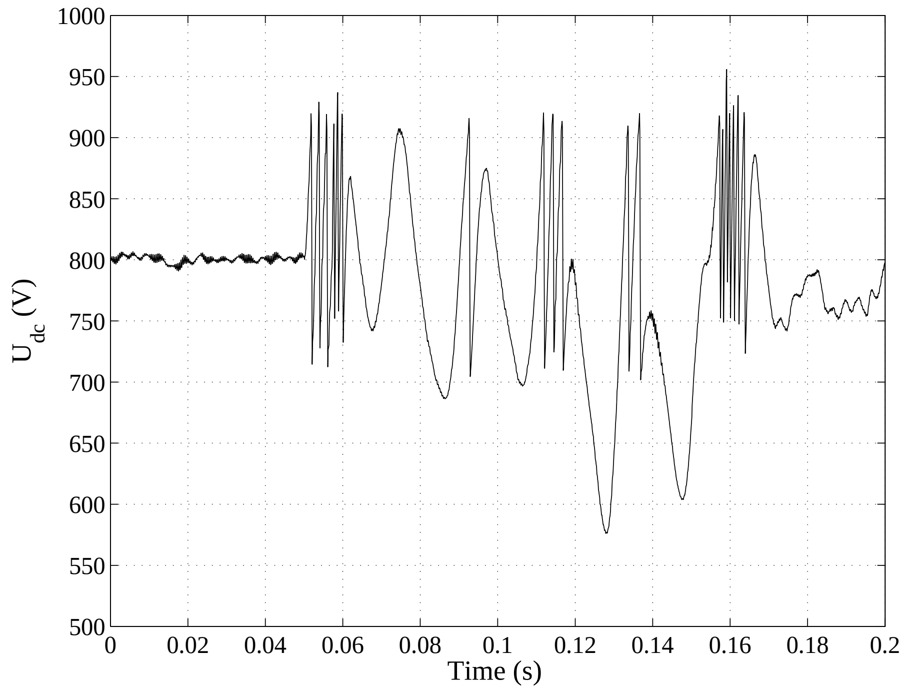

Figure 8.6: DC-link voltage during the synthetic voltage dip.

8.2 Simulation of response to "limit dip" for small wind energy facilities

In Fig. 8.7 the voltages making up the "limit dip" for small wind farms are presented. The turbine is operating slightly below rated power.

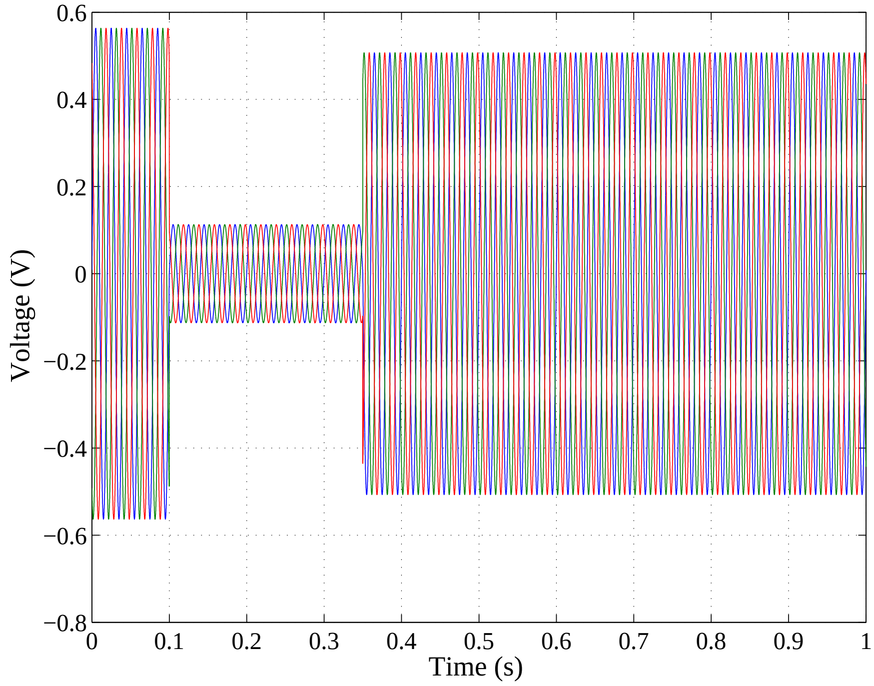

Figure 8.7: Voltages during the "limit" dip for small wind energy installations stated by SvK.

This causes a high power to flow through the rotor converter and into the dc-link, which can be noted in Fig. 8.8 where the active and reactive rotor powers are displayed.

This large power inflow of course cause a very large impact on the dc-link protective circuit. In Fig. 8.9 it can be noted that the dc-link voltage increases frequently due to the very high power that now come from the rotor converter and in Fig. 8.10 it can be noted that the dc-link crowbar now must be very active.

The result is that the system very well manages to control the turbine which can be observed in Fig. 8.11 where the resulting active and reactive power out to the grid are presented.

It can be noted that the proposed simulation strategy well manages to keep the turbine on-line and quickly recover after the fault.

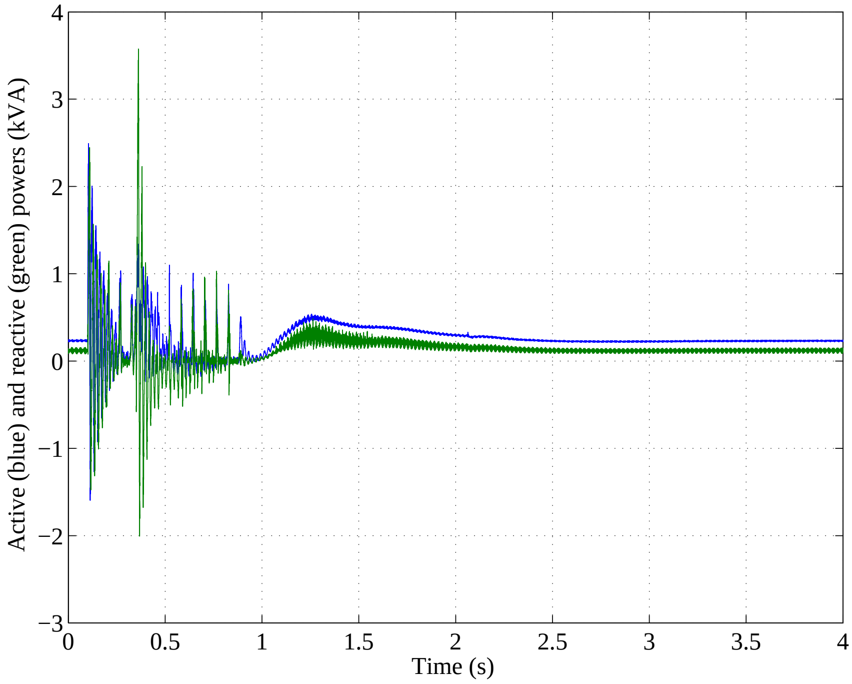

Figure 8.8: Active (blue) and reactive (green) rotor powers during the "limit dip" for small wind energy installations.

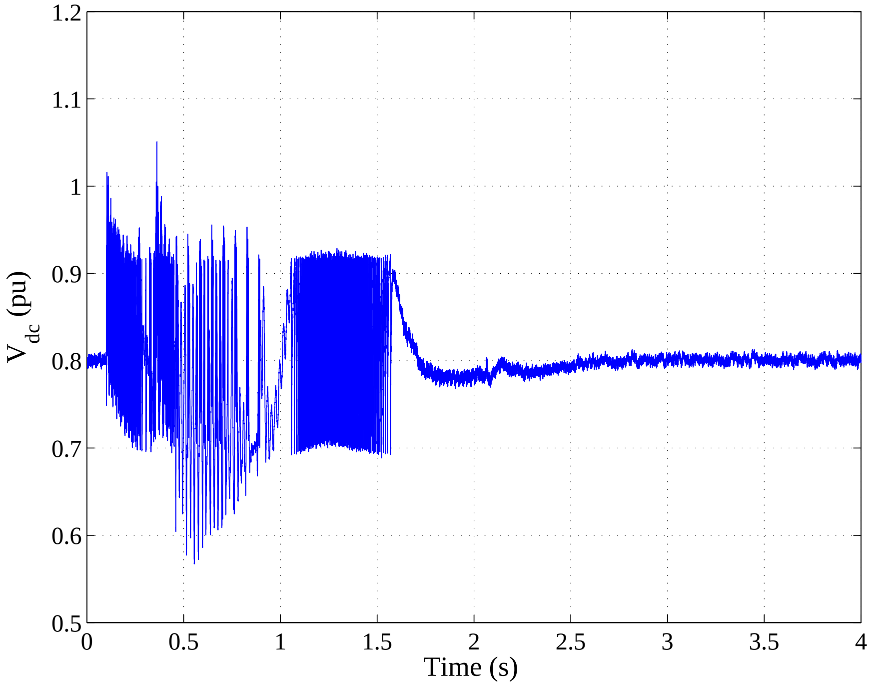

Figure 8.9: DC link voltage during the "limit" dip for small wind energy installations stated by SvK.

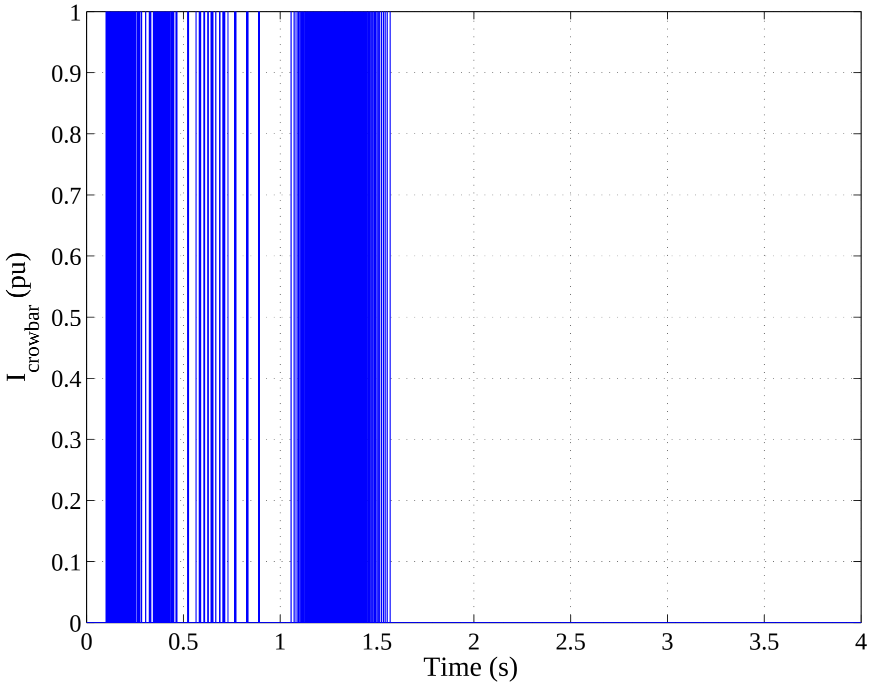

Figure 8.10: DC crowbar current during the "limit" dip for small wind energy installations stated by SvK.

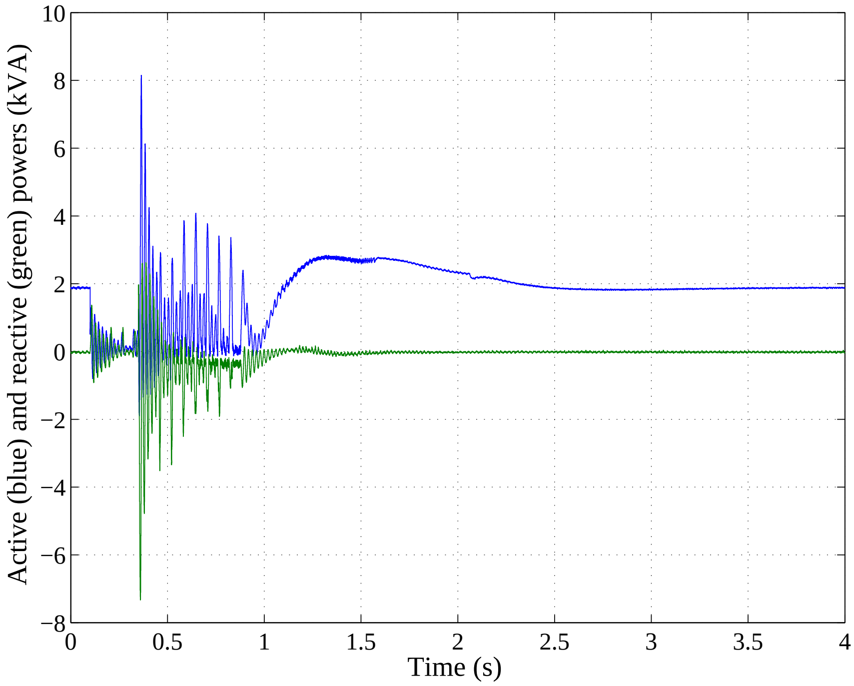

Figure 8.11: Active power (blue) and reactive power (green) during the "limit" dip for small wind energy installations stated by SvK.

8.3 Simulation of response to "limit dip" for large wind energy facilities

In Fig. 8.12 the voltages making up the "limit dip" for large wind farms are presented.

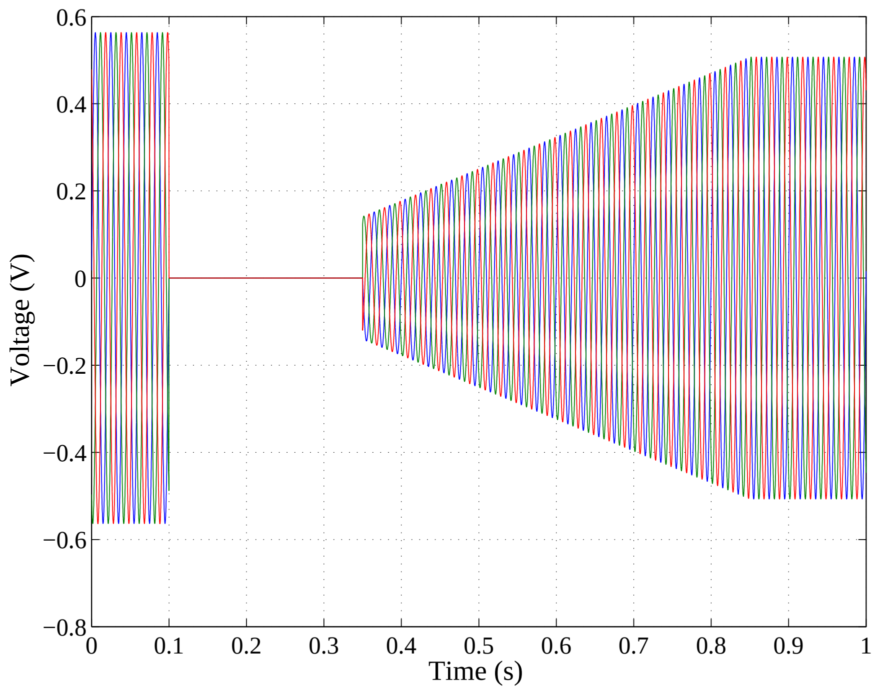

Figure 8.12: Voltages during the "limit" dip for large wind energy installations stated by SvK.

Again, the large inflow of power from the rotor causes the dc-link protective circuit to act due to the over voltage that otherwise would occur. In Fig. 8.13 the dc-link voltage is presented and in Fig. 8.14 the dc-link crowbar current.

Finally, in Fig. 8.15 the resulting active and reactive power out to the grid are presented. After some transients, the system manages to return to a stable operation.

It can be noted that the proposed simulation strategy well manages to keep the turbine on-line and quickly recover after the fault.

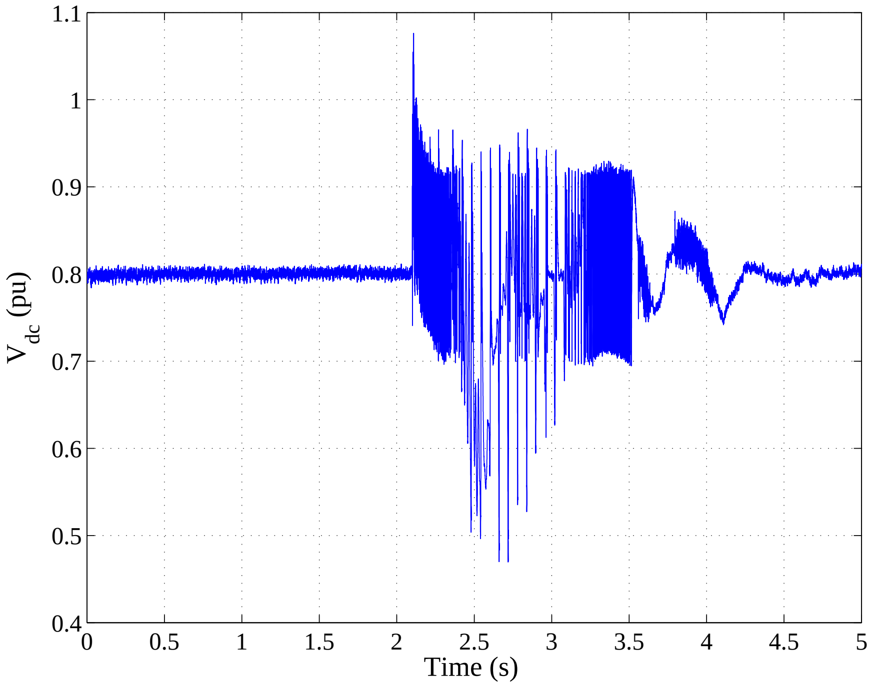

Figure 8.13: DC link voltage during the "limit" dip for large wind energy installations stated by SvK.

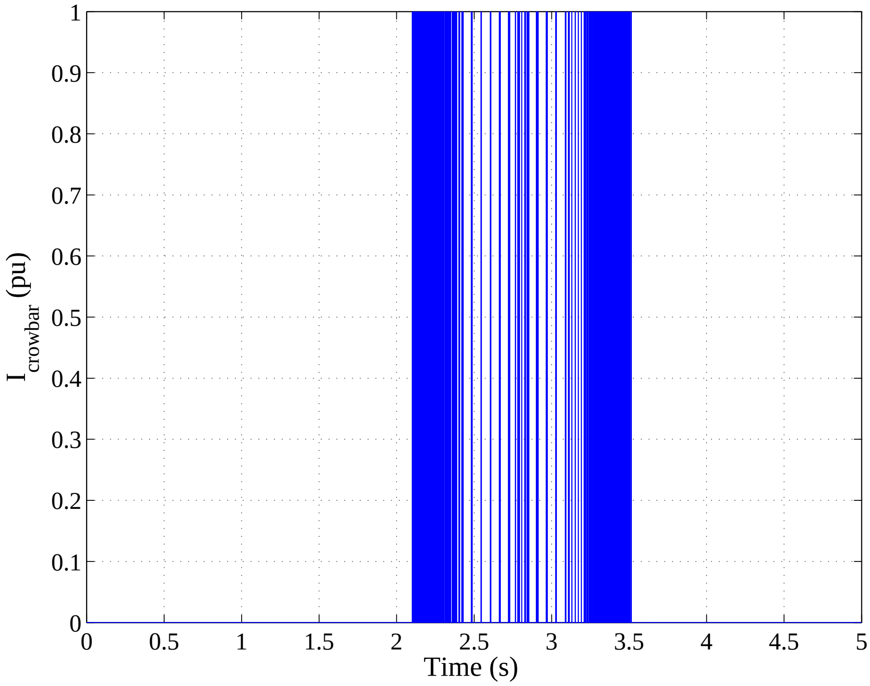

Figure 8.14: DC crowbar current during the "limit" dip for large wind energy installations stated by SvK.

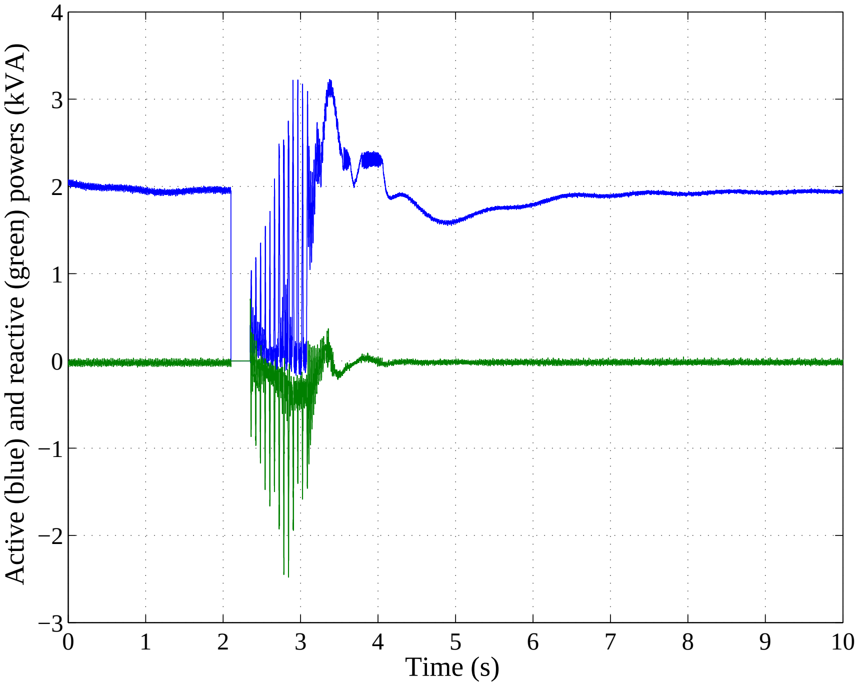

Figure 8.15: Active power (blue) and reactive power (green) during the "limit" dip for large wind energy installations stated by SvK.

Chapter 9

Comparisons between measured and simulated behaviour

9.1 Severe voltage dip to almost 0 % on July 12 2008

The most severe dip occurred on the 12th of July at 16.03. The voltage during this occasion is shown in Fig. 9.1. It can be noted that the voltage is almost zero for a period of 70 ms.

The active and reactive powers coming from the stator are presented in Fig. 9.2 and in Fig. 9.3. During the voltage dip, there is an excellent agreement between the measured stator power and the simulation, even though the disturbance is severe. However, after the dip has ceased, there is a substantial difference in the performance. This should not be surprising since, the simulations have been performed using a completely generic model. It should be pointed out that in both in the measurement and the simulation, the DFIG system rides through the dip without any larger problems.

The active and reactive powers coming from the rotor are presented in Figs. 9.4 and 9.5.

The active and reactive powers coming from the converter are presented in Figs .9.6 and 9.7.

Here the agreement is less good between measurements and simulation. One reason is that the turbine, for some reason, seems to be operating at a subsynchronous speed when the dip comes, even though for this power level it should be operating at supersynchronous speed. This is most evident in Figs. 9.6 and 9.4 where the difference in the converter power direction between measurement and simulation is obvious.

The measured and simulated DC-link voltages are presented in Fig. 9.8

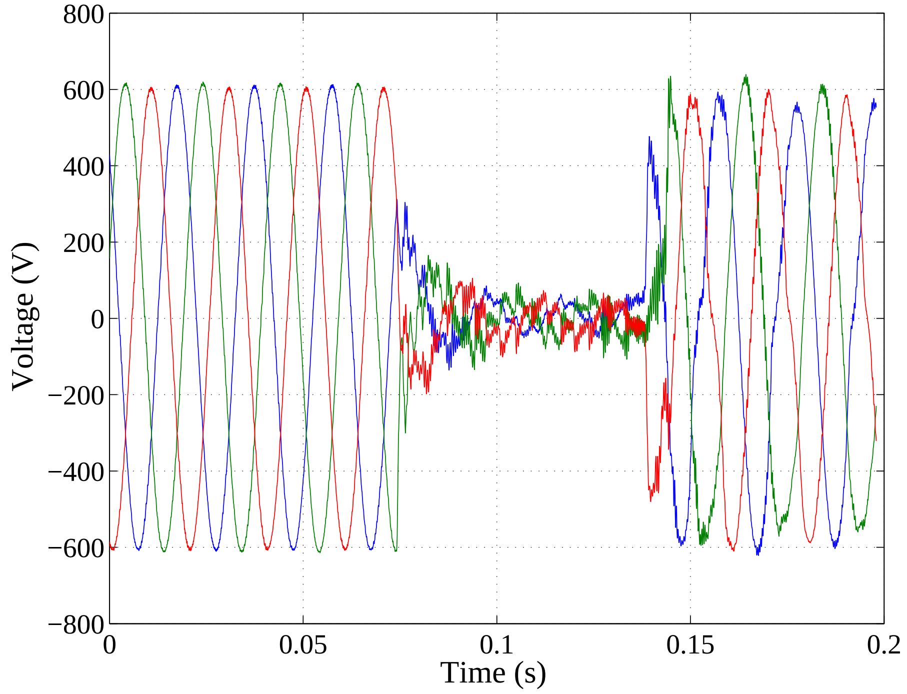

Figure 9.1: Voltage dip registered 12th of July 2008 at 16.03.

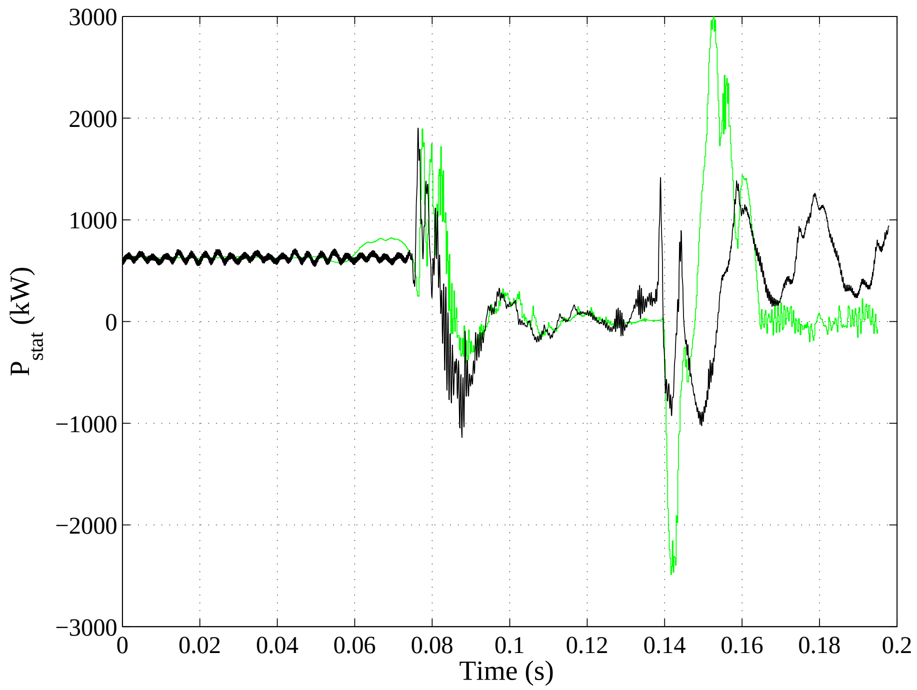

Figure 9.2: Stator active power: measured (black) and simulated (green).

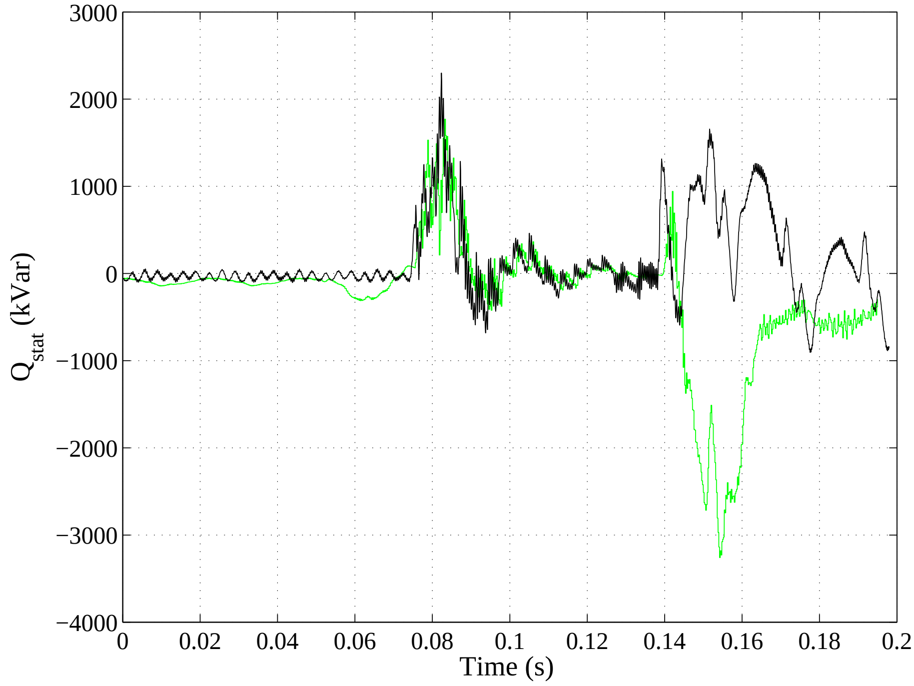

Figure 9.3: Stator reactive power: measured (black) and simulated (green).

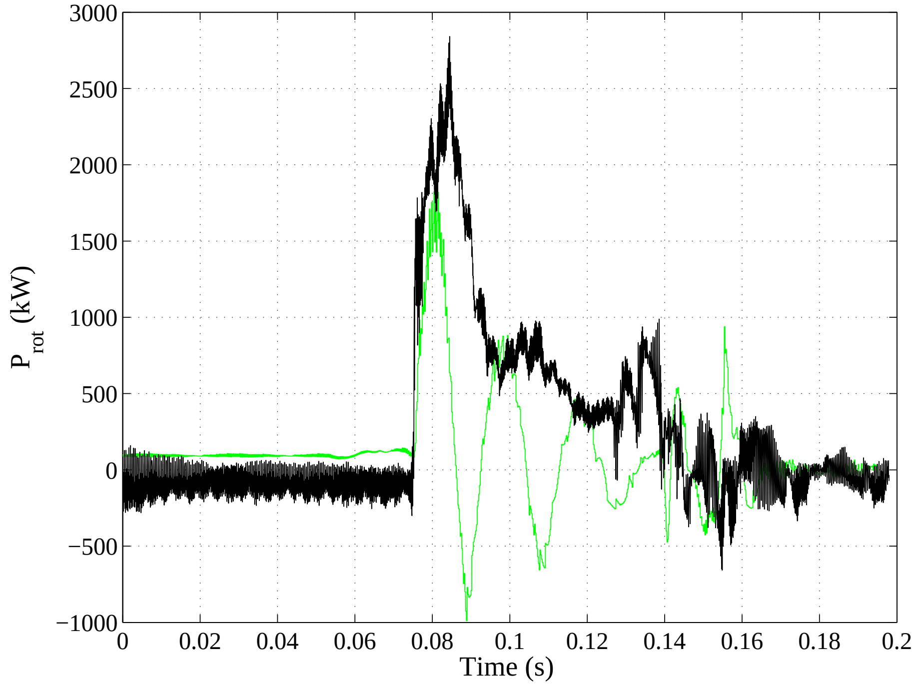

Figure 9.4: Rotor active power: measured (black) and simulated (green).

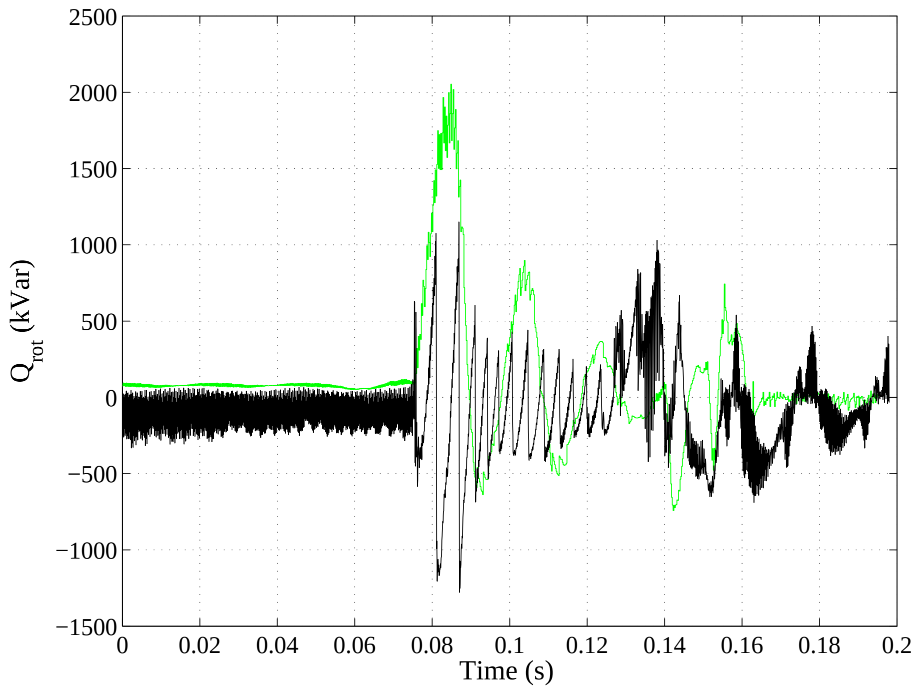

Figure 9.5: Rotor reactive power: measured (black) and simulated (green).

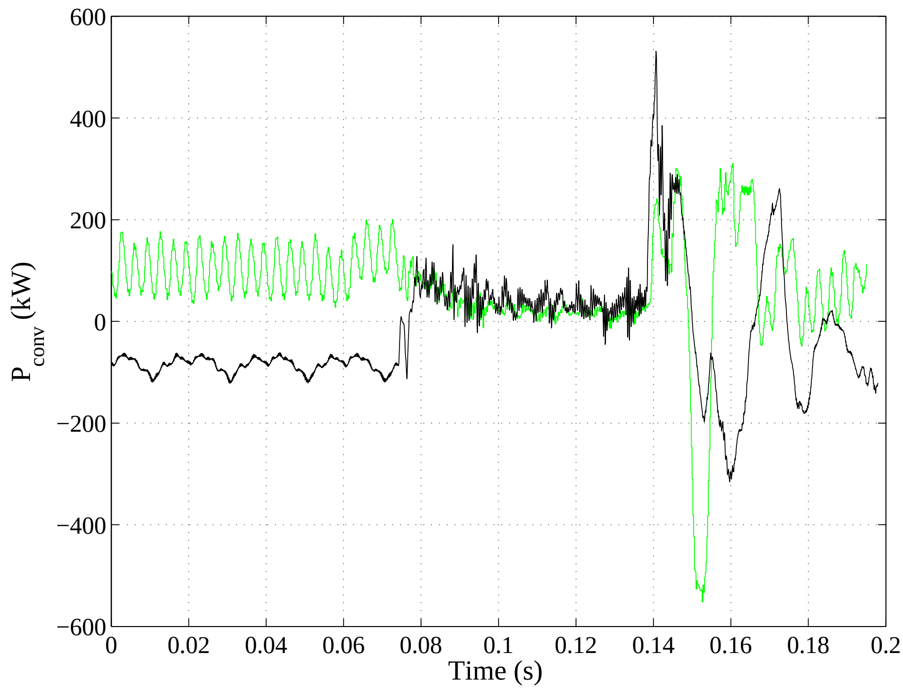

Figure 9.6: Converter active power: measured (black) and simulated (green).

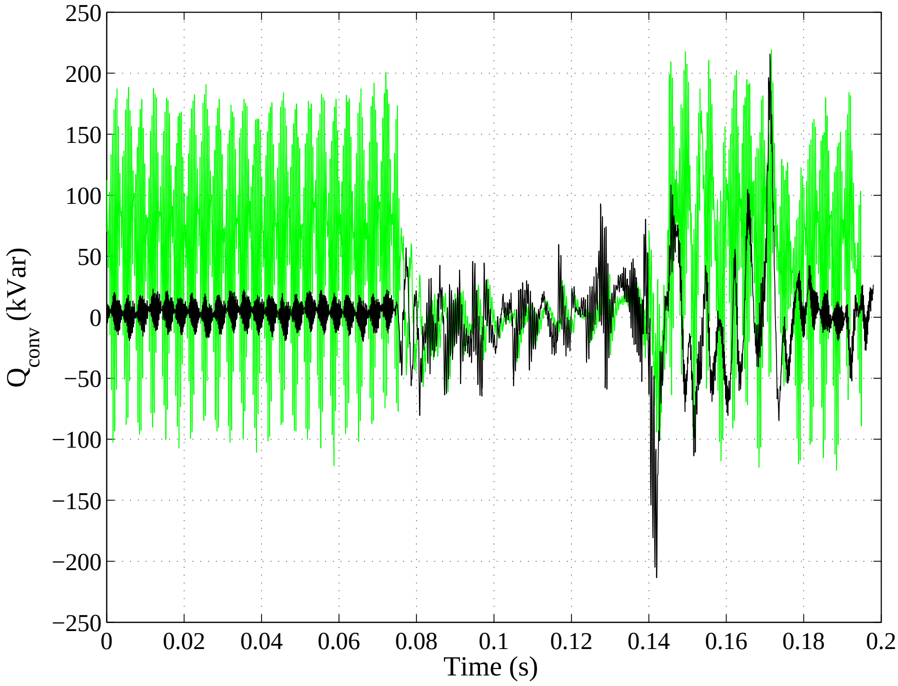

Figure 9.7: Converter reactive power: measured (black) and simulated (green).

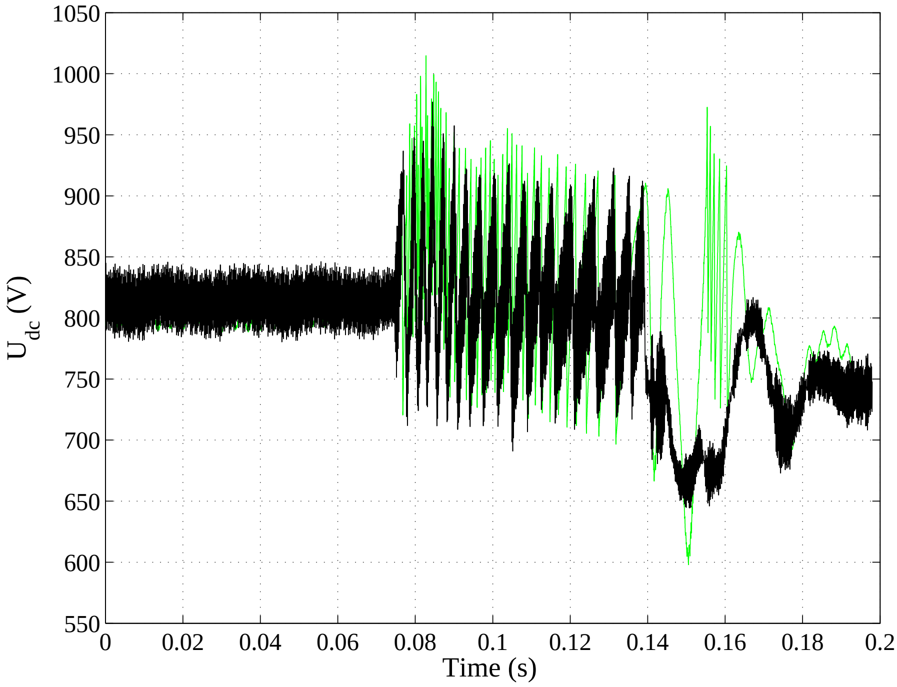

Figure 9.8: DC-link voltage, measured (black) and simulated (green)

The high power flowing into the rotor makes the DC-link voltage to rise quickly. In order to prevent damage to the DC-link capacitor and the transistors of the converters, the DC-link crowbar activates, keeping the DC-link voltage within acceptable voltage levels. The measured current through the DC crowbar is presented in Fig. 9.9 and the simulated one is presented in Fig. 9.10

The performance of the ride-through functionality is as desired, in the simulations as well as in the measurements. It can be noted that the agreement between measurements and simulations is very good during the voltage dip, but then differs once the dip has been cleared.

The voltage recovers quickly when the fault has been cleared, see Fig. 9.11. However, there is a small asymmetry in the voltages after the dip.

In Figs. 9.12 and 9.13 the total active and reactive powers from the turbine are presented.

It can be noted that the turbine in reality very quickly returns to the original state without any larger swings. However, in the simulations there are some swings lasting for a longer while. These demonstrates, that there ares some potential for improvement of the model. One possible reason for the behavior is that in the model used in this work there is no handling of the

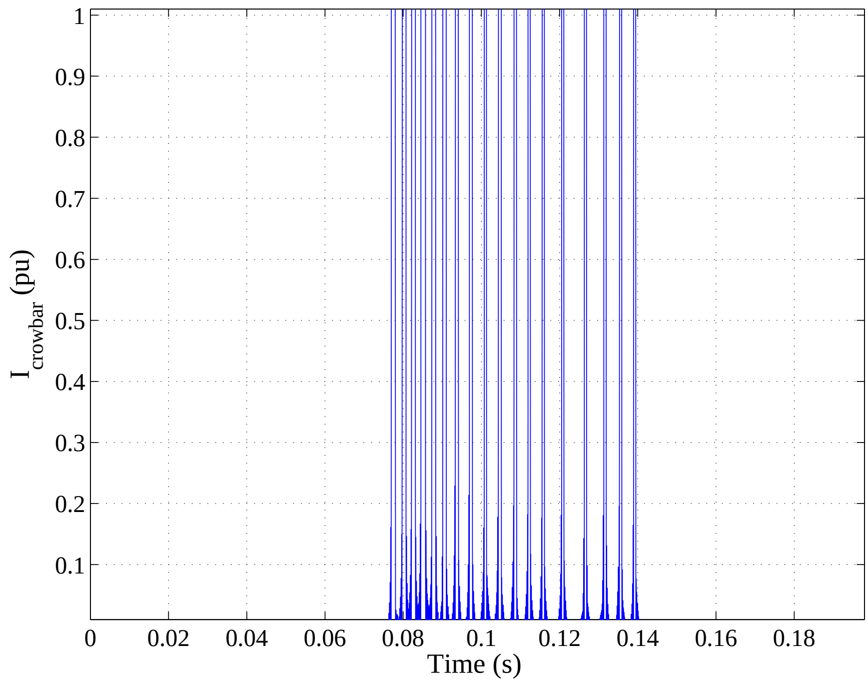

Figure 9.9: measured crowbar current in pu.

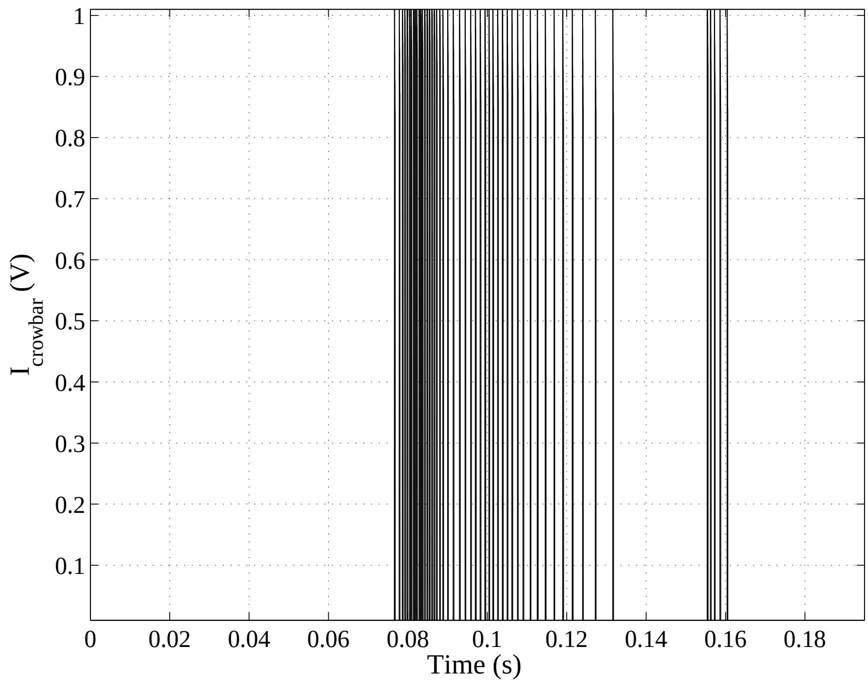

Figure 9.10: Simulated crowbar current in pu.

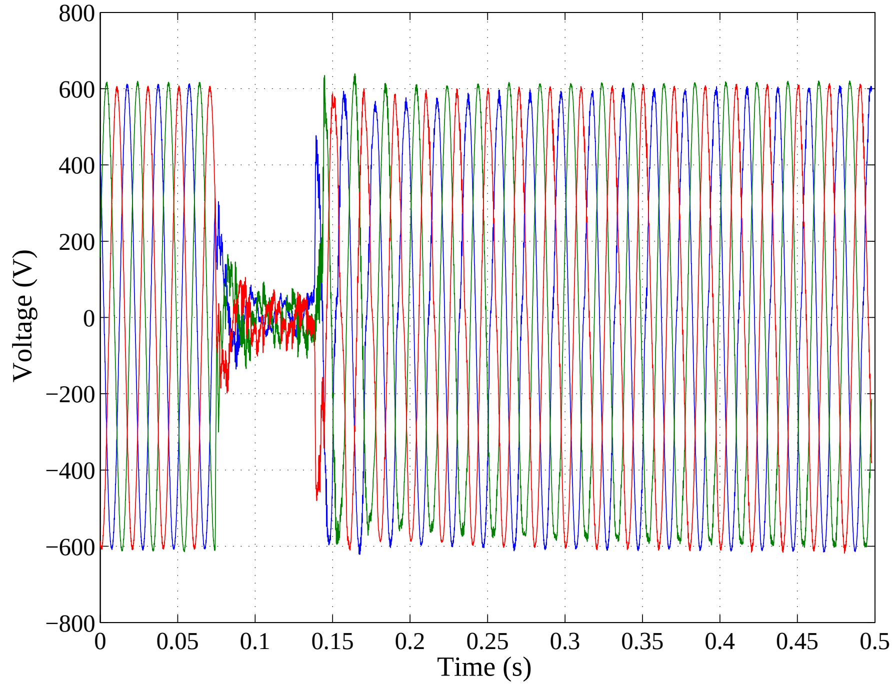

Figure 9.11: Voltage during the occasion on July the 12th.

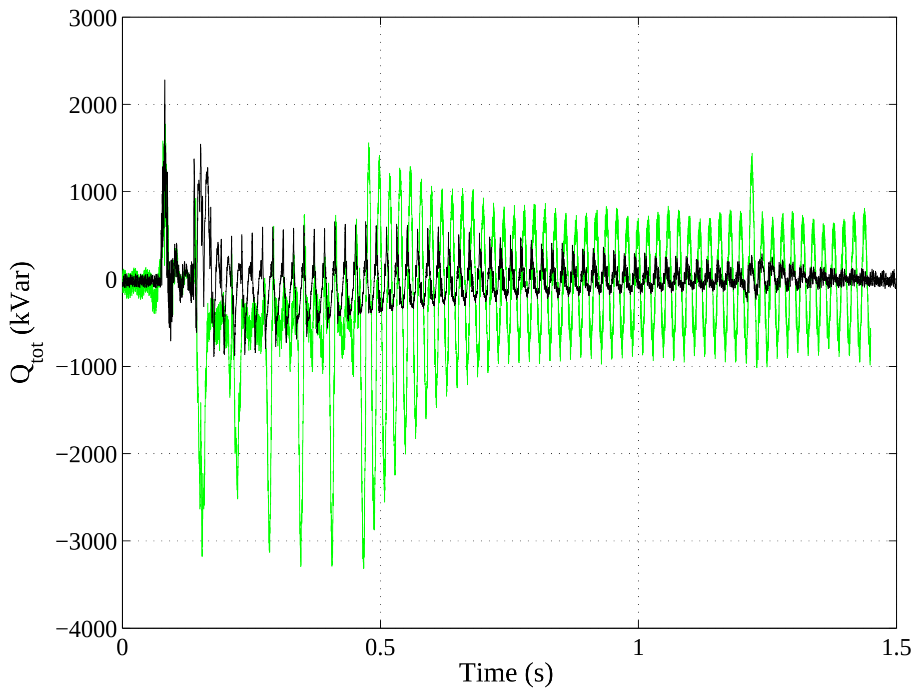

Figure 9.12: Reactive power the occasion on July the 12th.

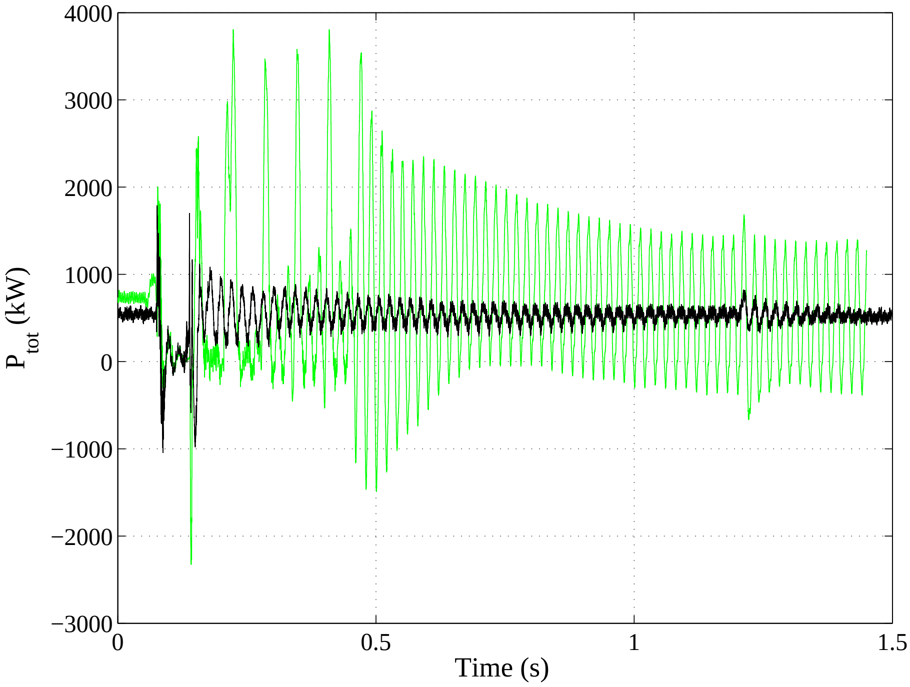

Figure 9.13: Active power during the occasion on July the 12th.

negative sequence, which could be the reason for the oscillations, occurring in particular in the long-term reactive current response.

9.2 Asymmetric dip on July 19 2008

An asymmetric dip occurred on the 19th of July at 16.05. The voltage during this occasion is shown in Fig. 9.14. It can be noted that the voltage in one of the phases is higher than in the other two ones.

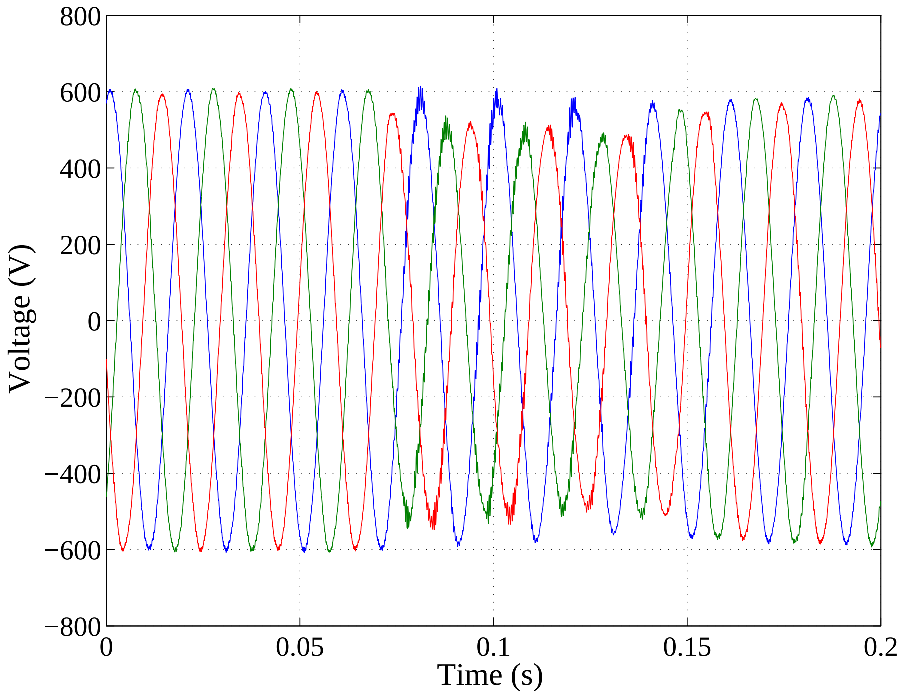

Figure 9.14: Voltage dip registered 19th of July 2008 at 16.05.

The active and reactive powers coming from the stator are presented in Fig. 9.15 and in Fig. 9.16.

The behavior of the simulations are in this case more oscillatory compared to the measurements. Again, the fact that no negative sequence control is made in the generic model could be a reason for the fairly large power oscillations.

The active and reactive powers coming from the rotor are presented in Figs. 9.17 and 9.18 and here the agreement is very good.

The active and reactive powers coming from the converter are presented in Figs. 9.19 and 9.20. The results are not exactly the same, but similar.

The measured and simulated dc link voltage are presented in Fig. 9.21. Here the consequence of the more oscillatory behavior in the simulations are visible, as larger oscillations on the dc-link.

And a further result in line with this can be observed in Figs. 9.22 and

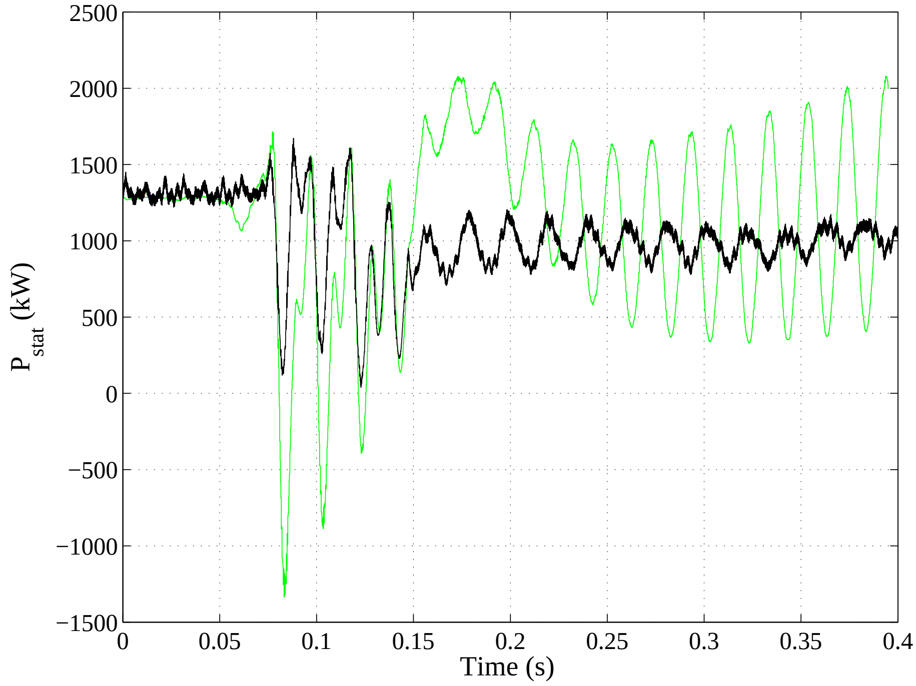

Figure 9.15: Stator active power, measured (black) and simulated (green).

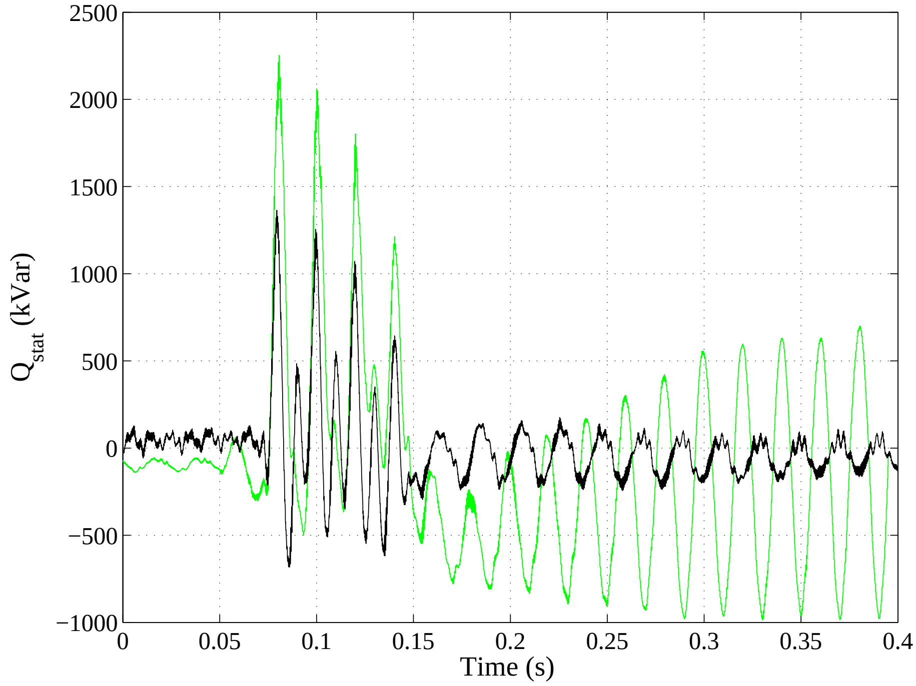

Figure 9.16: Stator reactive power measured (black) and simulated (green).

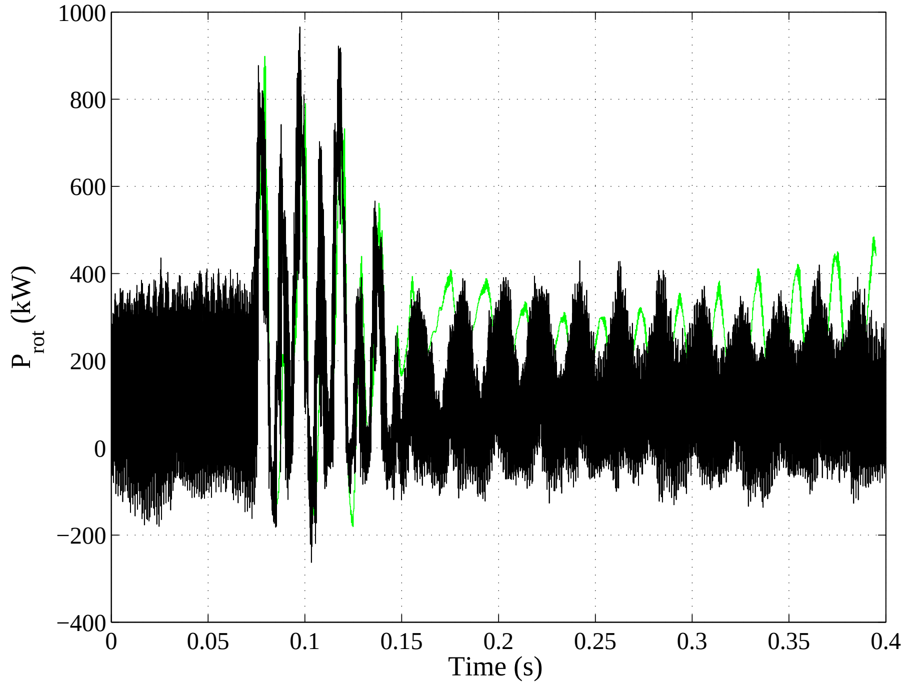

Figure 9.17: Rotor active power, measured (black) and simulated (green).

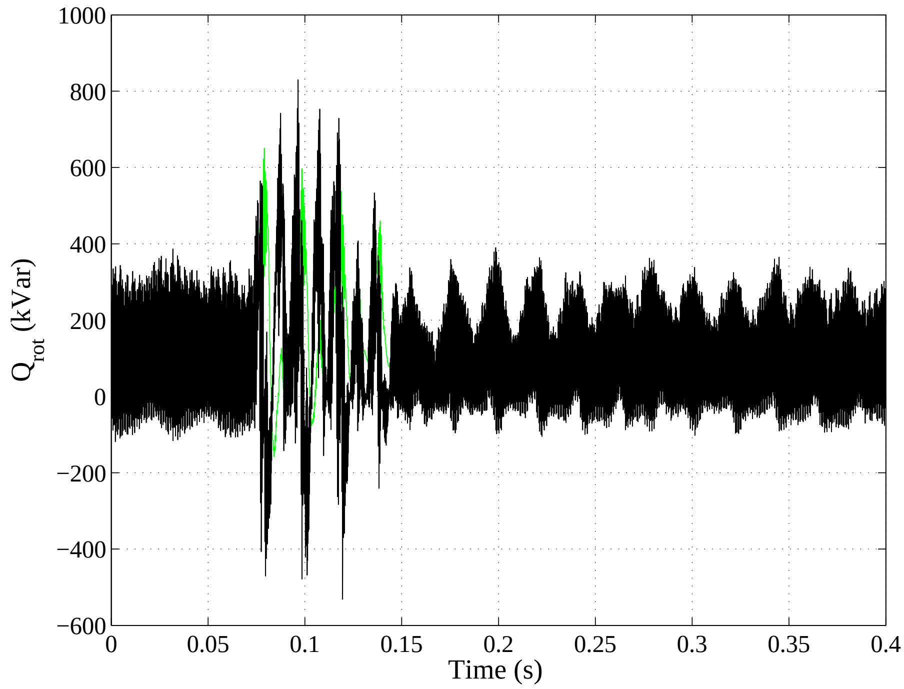

Figure 9.18: Rotor reactive power, measured (black) and simulated (green).

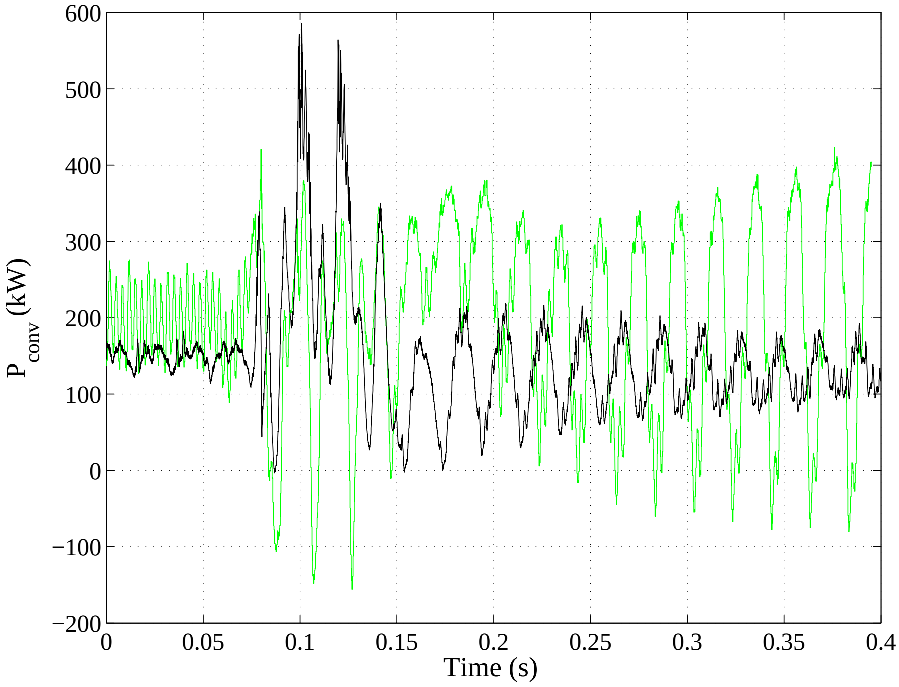

Figure 9.19: Converter active power, measured (black) and simulated (green).

9.23 where the measured and simulated dc crowbar currents are presented. Due to the larger swings in the simulation, the dc crowbar in the simulations operates more times.

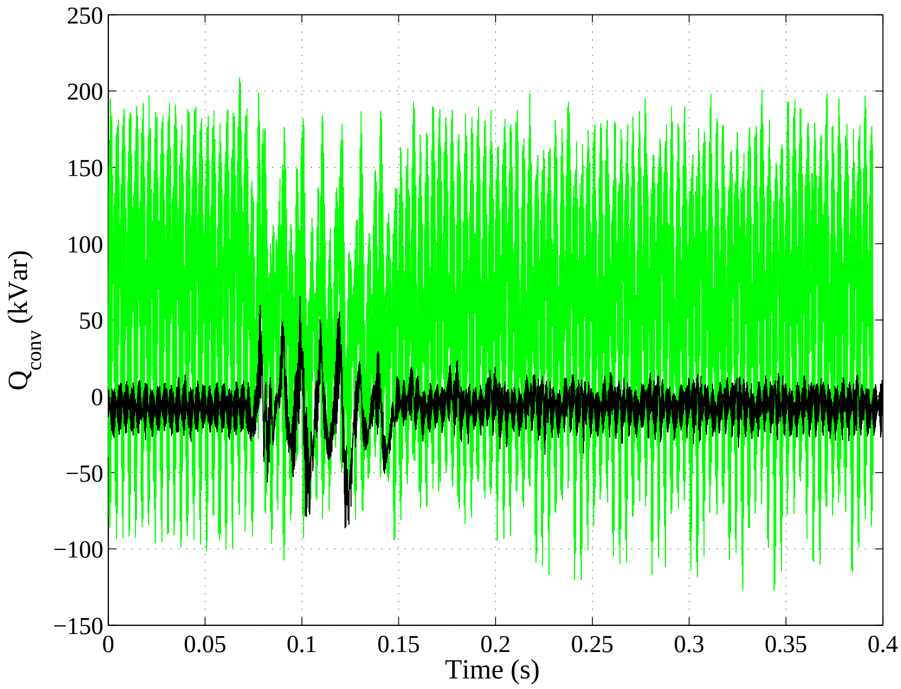

Figure 9.20: Converter reactive power, measured (black) and simulated (green).

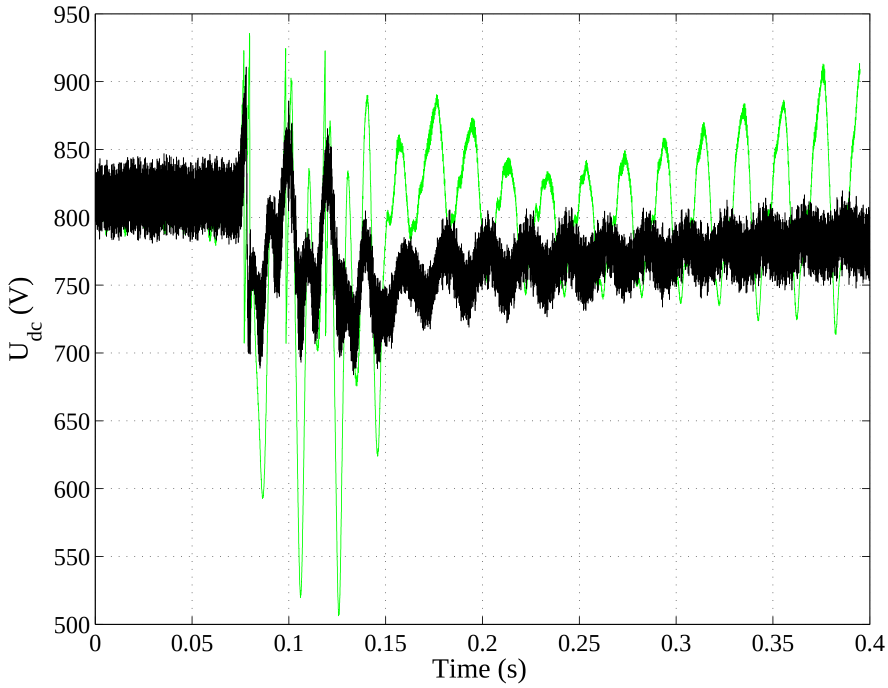

Figure 9.21: Dc link voltage, measured (black) and simulated (green)

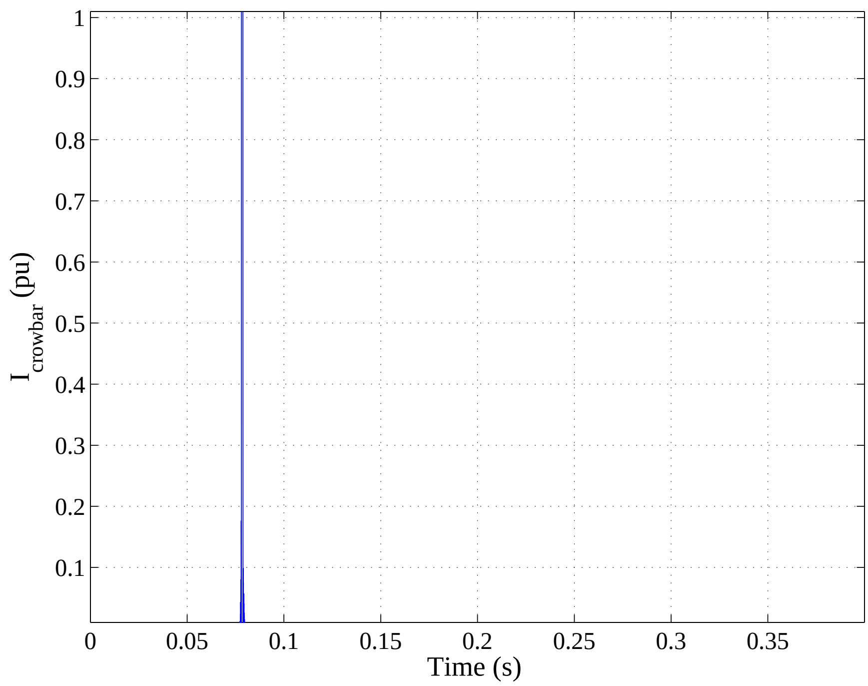

Figure 9.22: Measured crowbar current in pu.

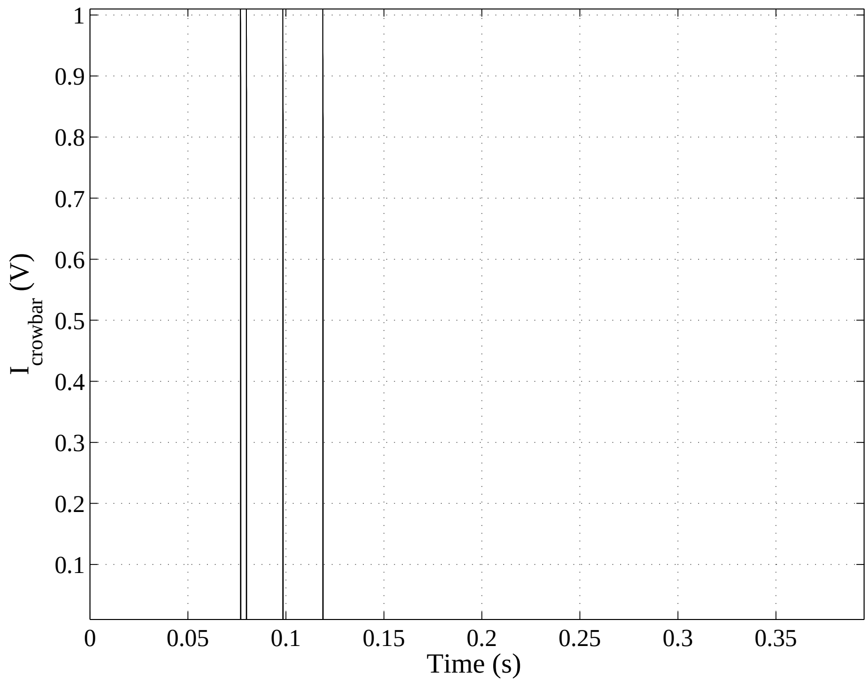

Figure 9.23: Simulated crowbar current in pu.

Chapter 10

Conclusions

A measurement and monitoring program conducted on a 2MW DFIG wind turbine equipped with voltage ride-through functionality has verified that the turbine has the desired behavior. The turbine was a Vestas 2 MW turbine equipped with AGO2. The undervoltage immunity required by SvK (Svenska Kraftnät) is provided by the added equipment.

During the period May 2008 to December 2008 several dips occurred, the most severe one reaching less than 10 % remaining voltage. The turbine managed to ride through all of these dips.

Moreover, the generic model of a DFIG turbine presented in this report predicts similar behavior as that of the real turbine. This is true even for the most severe voltage dip, which was examined as an example.

Finally voltages following the undervoltage limit curves stated by SvK was subjected to the simulated system, and the result was that the simulated system could well handle these disturbances

References

[1] IEC standard 61400-21, 2000-11-15, *Draft IEC 61400-21, Ed.1: Wind turbine generator systems- Part 21: measurements and assessment of power quality characteristics of grid connected wind turbines.*

[2] IEC standard 61000-4-15, 1997-11, *IEC 61000-4-15, Electromagnetic compatibility (EMC) - Part 4: Testing and measurement techniques - Section 15: Flickermeter - Functional and design specifications.*

[3] *Anslutning av Mindre Produktionsanläggningar till elnätet (AMP)*, Sveriges ellevarantörer, 1999, (in Swedish)

[4] Swedich standard SS-EN 50160, *Voltage characterisitcs of electricity supplied by public distribution systems.*

[5] Harnefors, L., *Control of Variable-Speed Drives*, Course Compendium, Mälardalen University, September 2002.

[6] Petersson, A., Harnefors, L., Thiringer, T., *Comparison Between Stator-Flux and Grid-Flux Oriented Rotor-Current Control Of Doubly-Fed Induction Generators*, Proc. IEEE Power Electronics Specialists Conference (PESC'04), Vol. 1, Aachen, Germany , June 20-25, 2004, pp. 482-486.

[7] Petersson, A. *Analysis, Modeling and Control of Doubly-Fed Induction Generators for Wind Turbines*, Chalmers University of Technology, Thesis for the degree of Doctor of Philosophy, 2005. ISBN 91-7291-600-1.

[8] Fortescue, C. L., *Method of symmetrical co-ordinates applied to the solution of polyphase networks*, 34th Annual Convention of the American Institute of Electrical Engineers, June 28, 1918.

[9] Slemon, G. R. *Modelling of induction machines for electric drives*, IEEE transactions on Industry Applications, Vol. 25, No. 6, pp. 1126 - 1131, November/December 1989.

[10] Petersson, A., Harnefors, L., Thiringer, T., *Evaluation of current control methods for wind turbines using doubly-fed induction machines*, IEEE Transactions on Power Electronics, Vol. 20, No. 1, pp. 227 - 235, January 2005.

[11] Harnefors, L., Bongiorno, M., Lundberg, S., *Input-Admittance Calculation and Shaping for Controlled Voltage-Source Converters*, IEEE transactions on Industrial Electronics, Vol. 54, No. 6, pp. 3323 - 3334 , December 2007.